injected to the mice through the polyethylene tubing line. The pharmacokinetics of the nanoparticles was repeatedly monitored by MRI measurements for 5 hours.

Two dimensional T1-weighted multi-slice spin echo MRI with fat suppression was performed with the following parameters: TR = 476 ms, TE = 9.57 ms, matrix size = 256 × 256, FOV = 3.2 × 3.2 mm^2, slice thickness (ST) = 1.0 mm, scan time 8 min 8 s, and number of acquisitions (NA) = 4. Slice orientation was horizontal (eight slices, gap 1 mm).

In vivo fluorescence imaging of nanoparticles

In vivo fluorescence imaging was performed before or 15, 30, 90, and 180 min after intravenous injection (100 μL) of Alexa 647-nanoparticle to the mice. Images were acquired using a fluorescent imager (Maestro EX, PerkinElmer) with the following parameters: excitation filter = 576–621 nm; emission filter = 635 nm longpass; acquisition setting = 630–800 nm in 10 nm steps; acquisition time = 100 ms; and FOV = 12.0 × 12.0 cm^2. Prior to and during the MRI scan, all mice were anaesthetized through a facemask with 2.0% isoflurane (Mylan Japan, Tokyo, Japan). The mice were put in a clean cage during the optical imaging and the urine was collected from the cage at the corresponding time. The mice were sacrificed after the 180 min-scanning and the main organs were collected, followed by measurement of their fluorescence by Maestro EX. After acquisition, unmixed fluorescence information was extracted from the fluorescence spectrum using the Maestro software package (PerkinElmer).

Results and discussion

Effect of encapsulated molecules on nanoparticle formation

First we prepared three types of nanoparticles containing dual probes: (1) nanoparticles with Alexa 647 and ferritin encapsulated chemically and physically, respectively; (2) nanoparticles with Flu and Dex-Mn encapsulated chemically and physically, respectively; and (3) nanoparticles with Flu and trypsin encapsulated chemically and physically, respectively. Fig. 1a shows the results of DLS diameter measurements of the three types of nanoparticles. Although the size distributions of these nanoparticles were different, the average diameters of these nanoparticles were all in the range of 150–300 nm. Since the encapsulation of the various probe molecules did not appear to substantially affect nanoparticle diameter, we concluded that our method could be used to prepare ~200 nm nanoparticles containing various compounds.

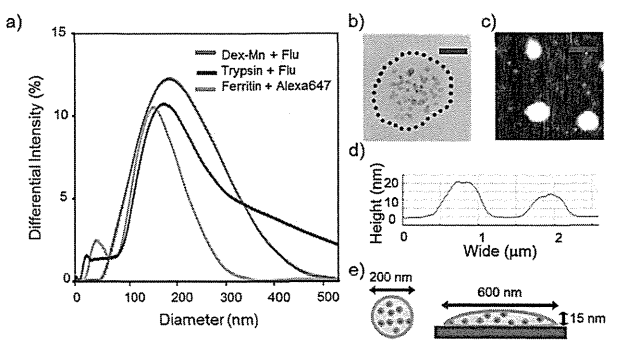

Fig. 1 (a) DLS measurements of the three types of nanoparticles prepared in this study, (b) TEM image of a nanoparticle containing ferritin, scale bar = 200 nm (c) AFM phase contrast image of the nanoparticles, scale bar = 1000 nm (d) cross-sectional topological profile obtained from image (c), and (e) schematic images of a nanoparticle dispersed in solution and of a nanoparticle affixed to a plate.

The diameter and shape of nanoparticles containing ferritin were examined by means of TEM and AFM (Fig. 1b and c). Interestingly, all the nanoparticles were observed to be round, with sizes in the range of 600–800 nm, which was 3 to 4 times the diameter measured by DLS (Fig. 1a). Three dimensional detailed AFM measurement showed the height of the nanoparticle was only 15–20 nm (Fig. 1d). This large difference in measured diameter probably occurred due to the different states of the nanoparticles required by these measurement techniques: the PEG-based nanoparticles were dispersed in water for DLS measurements, but were dried and affixed to a plate for TEM and AFM measurements. Because the nanoparticles were very soft and flexible, we expected that their shape likely would have changed during the drying pretreatment for TEM and AFM analysis. As shown in Fig. 1e, the volume of a spherical particle of 200 nm diameter, which was the diameter estimated by DLS analysis, is similar to the volume of a dried, flattened particle with a diameter of 600 nm and height of 15 nm, as estimated by TEM and AFM analysis. We determined that the black spots observed in the TEM image of the nanoparticles (Fig. 1b) corresponded to encapsulated ferritin; TEM images of particles that did not contain ferritin did not contain such black spots. The existence of the iron contained in ferritin was also confirmed by ICP-AES analysis (ESI, Fig. 1†). The image indicated that the encapsulated ferritin existed not only on the surface of the nanoparticles but also inside the nanoparticles.

Next, the stability of the nanoparticles was examined. Fig. 2a shows DLS measurements of a disperse solution of nanoparticles-encapsulated trypsin acquired just after preparation and the next day. The nanoparticles' diameter remained largely unchanged for 2 days of refrigerated storage in solution. This result indicates that the nanoparticles were stable under these storage conditions, and that they did not aggregate or collapse. Next, the stability of the probe molecules was examined by filtering solutions of two different types of nanoparticles, one with Flu chemically encapsulated and another with Dex-Flu physically encapsulated, and separately measuring the fluorescence intensity of the nanoparticle fraction and filtrate. We presumed that if the encapsulated Flu or Dex-Flu was leaked from the nanoparticles, the fluorescence signal of the filtrate would increase. Fluorescence intensities of the filtrate and nanoparticle fractions were measured after shaking for 12 h at 37 °C in mice serum. Although about 80% fluorescence signal was detected from the nanoparticle fraction, only a small signal was detected from the filtrates of both nanoparticle samples (Fig. 2b). The signals of the filtrate fraction of the chemically encapsulated nanoparticles were smaller than those of the physically encapsulated nanoparticles, presumably because the cleavage of the chemical bond to leak Flu into the filtrate was more difficult to achieve than the physical leak of Dex-Flu from

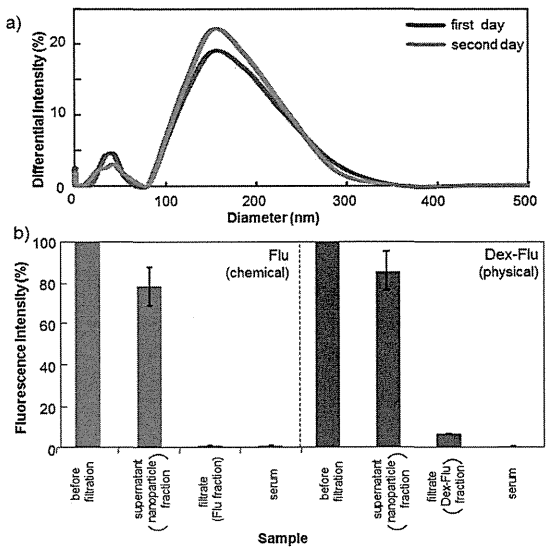

Fig. 2 (a) DLS measurements of a disperse solution of nanoparticles-encapsulated trypsin just after preparation and the next day, and (b) fluorescence analysis of nanoparticles modified either chemically (Flu, red bar) or physically (Dex-Flu, blue bar) with probe molecules after filtration.

its nanoparticles. The fluorescence intensity of the filtrate fractions was very small: the amounts of leaked Flu and Dex-Flu was negligible. These results indicate that both the nanoparticles and their encapsulated probe molecules were stable enough for further experiments.

Administration of nanoparticle-encapsulated Alexa 647 (chemically) and ferritin (physically) to mice

We used nanoparticles encapsulated with Alexa 647 and ferritin to study the nanoparticles' pharmacokinetics when administered to mice. Alexa 647, a fluorescent molecule with long excitation and emission wavelengths, is useful for monitoring the dynamics of nanoparticles within living mice. Because ferritin is an iron-storage protein that can be observed by TEM (Fig. 1b). It is a useful probe molecule for examining changes in the nanoparticles' shape upon excretion from the mice. The nanoparticles were administered *via* the mouse's coccygeal (tail) vein. The acute toxicity of the nanoparticles was negligible because no substantial changes in the blood pressure or heartbeat of the mice was observed after tail vein injection.

Although a strong fluorescence signal was detected in the bladder within 15 min of administration, no fluorescence signal was detected in other internal organs regardless of time, up to 180 min post-administration (Fig. 3a). The signal detected in the bladder increased with time, but disappeared after the mouse urinated (180 min). The collected urine was observed by TEM to observe excreted nanoparticles and ferritin (Fig. 3b). The shapes of the nanoparticles and the ferritin were similar to those observed in Fig. 1b. The distribution of ferritin within the nanoparticles (black dots in Fig. 3b) was similar to that observed prior to administration, as well. Therefore, we concluded that the nanoparticles had been excreted in the urine predominantly without changing form and without being

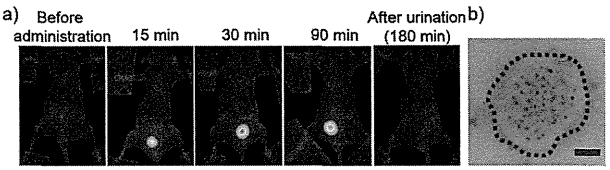

Fig. 3 (a) Fluorescence images of a mouse before and after administration of nanoparticles containing encapsulated ferritin and Alexa 647, and after urination, and (b) TEM image of a nanoparticle in mouse urine. Scale bar = 200 nm.

otherwise disturbed. In addition to containing clearly observable ferritin, the mouse urine also exhibited a fluorescence signal, demonstrating that both probes (ferritin and Alexa 647) remained within the nanoparticles when they were excreted. In general, nanoparticles less than 10 nm were excreted from urine,[17,18] however, nanoparticles with diameters greater than 10 nm are difficult to excrete in urine because the pore size of the kidney glomerulus is too small for penetration of these larger nanoparticles.[19] However, our results indicated that the 200 nm nanoparticles were excreted in urine; a similar phenomenon has been reported by He[20] and Lu,[21] who observed the excretion of 100 nm nanoparticles through mice urine. We hypothesized that the nanoparticles could change their shape to penetrate the kidney glomerulus, because the nanoparticles were very soft and flexible, as indicated by AFM images (Fig. 1c and d). More-detailed studies are needed to clarify the exact mechanism of excretion of the nanoparticles.

Administration of nanoparticle-encapsulated Flu (chemically) and Mn^{2+}-chelated compound (physically) to mice

Next, nanoparticles containing physically encapsulated Mn^{2+}-chelated compound and chemically encapsulated Flu were administrated to mice and were observed by means of MRI. MRI is a valuable diagnostic method for the observation of organs in living animals and humans,[22,23] and Mn^{2+} has recently received attention as an alternative MRI probe[24,25] because gadolinium (Gd^{3+}), the current standard MRI contrast agent, has been associated with nephrogenic systemic fibrosis.[26] On the other hand, low concentration of Mn^{2+} is considered as non toxic, because Mn^{2+} is an endogenous compound. To prevent leakage of Mn^{2+} from the nanoparticles, Mn^{2+} was chelated to dextran-modified diethylene triamine pentaacetic acid before being encapsulated in the nanoparticles.

An MRI signal (image contrast) was detected in the mouse bladder 15 min after administration (Fig. 4a, top row), and the signal increased with increasing time up to 5 h. MRI signals were also detected in the liver and kidney after administration (Fig. 4a, bottom rows). These results indicate that nanoparticles containing Mn^{2+} served as an effective positive MRI contrast agent, which is preferable for the detection of small changes that are caused by disease. For the liver and kidney, the MRI signals increased rapidly after administration and reached maximum intensities at 15 min after administration. Then, the signal started to decrease (Fig. 4b). The nanoparticles were eliminated from liver more rapidly than they were eliminated

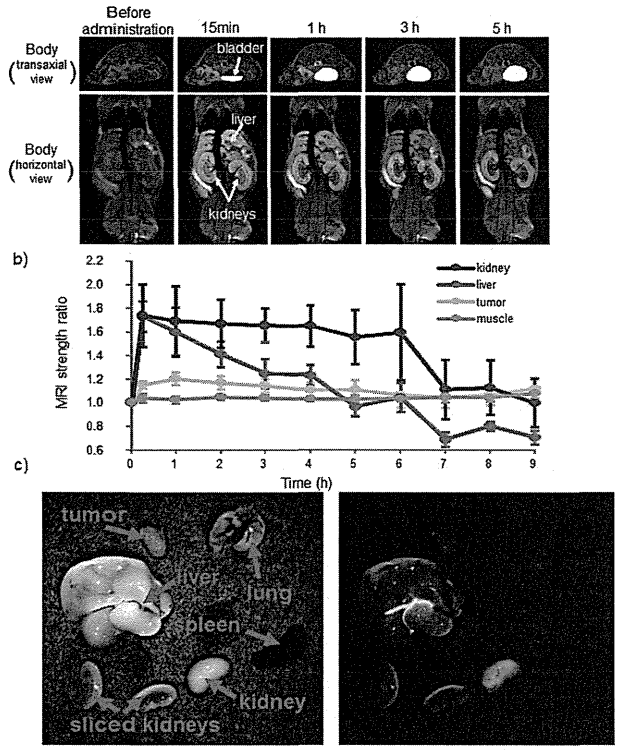

Fig. 4 (a) MRI images of a mouse before and after administration of nanoparticles containing encapsulated Mn^{2+} and Flu, (b) changes in MRI signal with increasing time post administration of the nanoparticles. The relative value was calculated from the equation (= MRI signal at the measured time/MRI signal before injection) (c) bright field and fluorescence images of organs 3 h after administration.

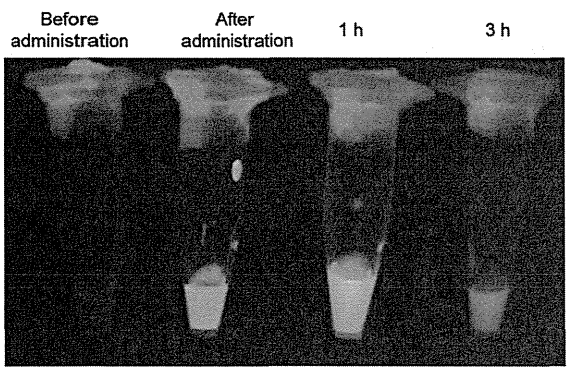

Fig. 5 Fluorescence images of urine collected from a mouse at different times before and after the administration of nanoparticles containing encapsulated Mn^{2+} and Flu.

from the kidneys. No obvious MRI signal enhancement was detected from other internal organs, including cancer tissue.

Although the fluorescence signal of Flu is hard to penetrate through the skin, the signal at *ex vivo* observation is more sensitive than an MRI signal. We therefore expected to see a small amount of nanoparticle accumulation in tissues or organs using *ex vivo* fluorescence analysis, after the *in vivo* study. The fluorescence signals of the internal organs and tissues of the mouse were analyzed 3 h after administration (Fig. 4c). Very strong fluorescence was observed in the bladder, and also a slight signal was observed in the liver and kidney; however, no signal enhancement was observed in the other organs such as cancer tissue, lungs, and spleen. This distribution of fluorescence signals corresponded with that observed for MRI signals in the same mouse, indicating that the two probes (Mn^{2+} and Flu) remained encapsulated within the nanoparticles and moved with the nanoparticles. Generally MRI is not highly sensitive for specific contrast agents (~μM), though it can be used to observe tissues deep within the body. On the other hand, fluorescence is highly sensitive *ex vivo* but cannot be used to observe tissues deep within the body. The combination of these two imaging techniques therefore can offer synergistic advantages over either modality used alone, and enables us to analyze the pharmacokinetics of nanoparticle distribution and excretion from the body in greater detail.

Strong fluorescence was detected from the urine that was collected from the mouse immediately after administration of the nanoparticles containing encapsulated Mn^{2+} and Flu (Fig. 5). This rapid excretion of nanoparticles in the urine was similar to the results observed for the nanoparticles containing ferritin and Alexa 647. (Fig. 3) Because both types of dual probes were excreted from the mice in a similar manner, we concluded that the composition of the encapsulated molecules did not affect the nanoparticles' distribution in, or rate of excretion from, the mouse's body. For this reason, we expect that a variety of probe molecules could be encapsulated within the soft PEG nanoparticles for use in animal experiments.

The nanoparticles were distributed mainly to the organs (bladder, kidney, and liver) that function to excrete dispensable or toxic compounds. Then, these nanoparticles were excreted quickly through the urine, along with the encapsulated probe molecules. Since the nanoparticles were excreted rapidly, the risk from compound where safety is a concern, like Gd^{3+}, will be reduced by encapsulation within the nanoparticles. In this report, we used non-targeting nanoparticles. It is expected that if active targeting of the nanoparticles to disease organs or tissues is achieved by the surface modification of the nanoparticle with targeting molecules (antibody, folate and so on) or changes to the nanoparticles size, the nanoparticles can be used as a theranostic tool.

Conclusions

In this study we developed a method to prepare soft PEG-based nanoparticles containing different probe molecules. The advantages of the nanoparticles were that (1) various probe molecules could be physically or chemically encapsulated within the nanoparticles, (2) different probe molecules were encapsulated within the nanoparticles simultaneously, (3) the nanoparticles could be detected in mice using various analytical techniques, depending on the type of probe molecules encapsulated, and (4) the soft nanoparticles were rapidly excreted through the urine, with low accumulation in the body. For these reasons, we concluded that these nanoparticles containing dual probes are promising for the reliable analysis of living animals.

Acknowledgements

We thank Dr S. Fukuda (UT), N. Nitta (NIRS), S. Shibata (NIRS), and S. Sakae (UT) for technical assistance with the TEM measurement, MRI measurement, for animal experiments, and for ICP-AES analysis, respectively. This work was supported by grants (Kakenhi) from the Ministry of Education, Culture, Sports, Science, and Technology (MEXT) of Japan, JSPS Core-to-Core Program, A. Advanced Research Networks, and the Naito Foundation. In addition, high-field MRI and optical imaging devices were supported by the Funding Program for World-Leading Innovative R&D on Science and Technology (FIRST Program).

References

1 J. Cheon and J.-H. Lee, *Acc. Chem. Res.*, 2008, **41**, 1630–1640.
2 L. E. Jennings and N. J. Long, *Chem. Commun.*, 2009, 3511–3524.
3 Y. Chang, Y. Li, X. Meng, N. Liu, D. Sun, H. Liu and J. Wang, *Polym. Chem.*, 2013, **4**, 789–794.
4 V. S. Talanov, C. A. S. Regino, H. Kobayashi, M. Bernardo, P. L. Choyke and M. W. Brechbiel, *Nano Lett.*, 2006, **6**, 1459–1463.
5 M. Higuchi, N. Iwata, Y. Matsuba, K. Sato, K. Sasamoto and T. C. Saido, *Nat. Neurosci.*, 2005, **8**, 527–533.
6 S. Mizukami, R. Takikawa, F. Sugihara, M. Shirakawa and K. Kikuchi, *Angew. Chem., Int. Ed.*, 2009, **48**, 3641–3643.
7 Y. Il Park, H. M. Kim, J. H. Kim, K. C. Moon, B. Yoo, K. Taek Lee, N. Lee, Y. Choi, W. Park, D. Ling, K. Na, W. K. Moon, S. H. Choi, H. S. Park, S.-Y. Yoon, Y. D. Suh, S. H. Lee and T. Hyeon, *Adv. Mater.*, 2012, **24**, 5755–5761.
8 J. Zhou, Y. Sun, X. Du, L. Xiong, H. Hu and F. Li, *Biomaterials*, 2010, **31**, 3287–3295.
9 A. B. Bourlinos, A. Bakandritsos, A. Kouloumpis, D. Gournis, M. Krysmann, E. P. Giannelis, K. Polakova, K. Safarova, K. Hola and R. Zboril, *J. Mater. Chem.*, 2012, **22**, 23327–23330.
10 A. Bumb, C. A. S. Regino and J. G. Egen, *Mol. Imaging Biol.*, 2011, **13**, 1163–1172.
11 S.-W. Chou, Y.-H. Shau, P.-C. Wu, Y.-S. Yang, D.-B. Shieh and C.-C. Chen, *J. Am. Chem. Soc.*, 2010, **132**, 13270–13278.
12 L. Shan, S. P. Wang, R. Sridhar, Z. M. Bhujwalla and P. C. Wang, *Mol. Imaging*, 2007, **6**, 85–95.
13 S. Murayama, B. Su, K. Okabe, A. Kishimura, K. Osada, M. Miura, T. Funatsu, K. Kataoka and M. Kato, *Chem. Commun.*, 2012, **48**, 8380–8382.
14 S. Murayama, T. Nishiyama, K. Takagi, F. Ishizuka, T. Santa and M. Kato, *Chem. Commun.*, 2012, **48**, 11461–11463.
15 S. Murayama, F. Ishizuka, K. Takagi, H. Inoda, A. Sano, T. Santa and M. Kato, *Anal. Chem.*, 2012, **84**, 1374–1379.
16 S. Murayama and M. Kato, *Anal. Chem.*, 2010, **82**, 2186–2191.
17 C. Eisner, H. Ow, T. Yang, Z. Jia, E. Dimitriadis, L. Li, K. Wang, J. Briggs, M. Levine, J. Schnermann and M. G. Espey, *J. Appl. Physiol.*, 2012, **112**, 681–687.
18 C. A. Simpson, K. J. Salleng, D. E. Cliffel and D. L. Feldheim, *Nanomed.: Nanotechnol., Biol. Med.*, 2013, **9**, 257–263.
19 M. Longmire, P. L. Choyke and H. Kobayashi, *Nanomedicine*, 2008, **3**, 703–717.
20 X. He, H. Nie, K. Wang, W. Tan, X. Wu and P. Zhang, *Anal. Chem.*, 2008, **80**, 9597–9603.
21 J. Lu, M. Liong, Z. Li, J. I. Zink and F. Tamanoi, *Small*, 2010, **6**, 1794–1805.
22 H. Kobayashi, S. Kawamoto, M. Bernardo, M. W. Brechbiel, M. V. Knopp and P. L. Choke, *J. Controlled Release*, 2006, **111**, 343–351.
23 A. B. Bourlinos, A. Bakandritsos, A. Kouloumpis, D. Gournis, M. Krysmann, E. P. Giannelis, K. Polakova, K. Safarova, K. Hola and R. Zboril, *J. Mater. Chem.*, 2012, **22**, 23327–23330.
24 A. C. Silva, J. H. Lee, I. Aoki and A. P. Koretsky, *NMR Biomed.*, 2004, **17**, 532–543.
25 I. Aoki, Y. J. L. Wu, A. C. Silva, R. M. Lynch and A. P. Koretsky, *NeuroImage*, 2004, **22**, 1046–1059.
26 H. S. Thomsen, *Radiol. Clin. North Am.*, 2009, **47**, 827–831.

BRAIN RESEARCH 1537 (2013) 350–355

Available online at www.sciencedirect.com

ScienceDirect

www.elsevier.com/locate/brainres

Brain Research

Research Report

Hemodynamic changes during neural deactivation in awake mice: A measurement by laser-Doppler flowmetry in crossed cerebellar diaschisis

Hiroyuki Takuwa[a], *Yosuke Tajima*[a], *Daisuke Kokuryo*[b], *Tetsuya Matsuura*[a,c], *Hiroshi Kawaguchi*[a], *Kazuto Masamoto*[a,d], *Junko Taniguchi*[a], *Yoko Ikoma*[a], *Chie Seki*[a], *Ichio Aoki*[b], *Yutaka Tomita*[e], *Norihiro Suzuki*[e], *Iwao Kanno*[a], *Hiroshi Ito*[a,*]

[a]*Department of Biophysics Program, Molecular Imaging Center, National Institute of Radiological Sciences, 4-9-1 Anagawa, Inage-ku, Chiba 263-8555, Japan*

[b]*Diagnostic Imaging Program, Molecular Imaging Center, National Institute of Radiological Sciences, 4-9-1 Anagawa, Inage-ku, Chiba 263-8555, Japan*

[c]*Academic Group of Mathematical and Natural Science, Iwate University, 4-3-5 Ueda, Morioka 020-8551, Japan*

[d]*Center for Frontier Science and Engineering, University of Electro-Communications, 1-5-1 Chofugaoka, Chofu, Tokyo 182-8585, Japan*

[e]*Department of Neurology, Keio University School of Medicine, 35 Shinanomachi Shinjuku-ku, Tokyo 160-8582, Japan*

ARTICLE INFO

Article history:
Accepted 18 September 2013
Available online 25 September 2013

Keywords:
Cerebellar blood flow
Red blood cell velocity
Red blood cell concentration
Neuronal deactivation
Awake animal
Crossed cerebellar diaschisis

ABSTRACT

Crossed cerebellar diaschisis (CCD) caused by contralateral supratentorial lesions can be considered a condition of neural deactivation, and hemodynamic changes in CCD were investigated with positron emission tomography (PET) in humans. In the present study, to investigate the effects of neural deactivation on hemodynamics, we developed a new mouse model of CCD, which was caused by middle cerebral artery occlusion (MCAO), and measured changes in cerebellar blood flow (CbBF), red blood cell (RBC) velocity and concentration due to CCD using laser-Doppler flowmetry (LDF) in awake mice. The ratio of the CCD side to the unaffected side in the cerebellum for CbBF 1 day after MCAO was decreased by −18% compared to baseline (before CCD). The ratio of the CCD side to the unaffected side for RBC concentration 1 day after MCAO was decreased by −23% compared to baseline. However, no significant changes in the ratio of the CCD side to the unaffected side were observed for RBC velocity. The present results indicate that the reduction of CbBF induced by neural deactivation was mainly caused by the decrease in RBC concentration. In contrast, our previous study showed that RBC velocity had a dominant role in the increase in cerebral blood flow (CBF) induced by neural activation. If RBC concentration can be considered an indicator of cerebral blood volume (CBV), hemodynamic changes due to neural activation and deactivation measured by LDF in mice might be in good agreement with human PET studies.

*Corresponding author. Fax: +81 43 206 0819.
E-mail address: hito@nirs.go.jp (H. Ito).

0006-8993/$ - see front matter © 2013 Elsevier B.V. All rights reserved.
http://dx.doi.org/10.1016/j.brainres.2013.09.023

1. Introduction

Positron emission tomography (PET) studies of the hemodynamics of crossed cerebellar diaschisis (CCD), which is caused by contralateral supratentorial lesions, have shown reductions in cerebral blood flow (CBF) and cerebral metabolic rate of oxygen ($CMRO_2$) in human (Lenzi et al., 1982; Martin and Raichle, 1983; Pantano et al., 1986; Yamauchi et al., 1992a, 1992b, 1999a, 1999b; Ito et al., 2002). CCD can be considered as neural deactivation (Ito et al., 2002), which is a reduction of neural activity as compared to the baseline level (spontaneous neural activity). In our previous study, we reported that hemodynamic changes in CCD measured with PET in humans showed almost the same degree of decrease in cerebral blood volume (CBV) and CBF (Ito et al., 2002). Animal studies, for which invasive procedures can be applied, can also be useful for investigating the mechanism of CCD resulting from neuronal deactivation. An anesthetized rodent model study reported the reduction of cerebellar blood flow (CbBF) associated with attenuation of spontaneous neural spiking activity, which was caused by middle cerebral artery occlusion (MCAO) and common carotid artery (CCA) occlusion (Gold and Lauritzen, 2002).

Recently, many investigators reported that anesthesia significantly affects the physiological states including the regulation of cerebral circulation throughout the brain (Martin et al., 2002, 2006; Lahti et al., 1999; Peeters et al., 2001; Sicard et al., 2003; Takuwa et al., 2011, 2012). Thus, we previously developed a system for measurement of cerebral hemodynamics in awake rodent using laser-Doppler flowmetry (LDF; Takuwa et al., 2011). Moreover, using this system, we investigated hemodynamic changes during neural activation in awake mice (Takuwa et al., 2012), and showed that the increase in red blood cell (RBC) velocity was far greater than that in RBC concentration and that it had a dominant role in the increase in CBF induced by neural activation.

On the other hand, hemodynamic changes caused by neuronal deactivation in awake animals was still unknown. To the best of our knowledge, no study has investigated the dynamics of RBC velocity and concentration independently in awake animals. In the present study, in order to investigate the effects of neural deactivation on hemodynamics, we developed a CCD mouse model caused by MCAO and measured changes in CbBF, a product of RBC velocity and concentration in cerebral microvessels, using LDF before and after neural deactivation under awake conditions.

2. Results

2.1. *Changes in CbBF and RBC velocity and RBC concentration during CCD*

Fig. 2 shows the percentage changes in the ratio of the CCD side to the unaffected side for CbBF and RBC velocity and concentration at one day after MCAO. The percentage changes in the ratio of CCD to the unaffected sides for CbBF, RBC velocity and concentration were $-18\pm11\%$, $5\pm14\%$ and $-23\pm17\%$, respectively. The percentage changes in the ratio of CCD to the unaffected sides for CbBF ($P<0.05$) and RBC concentration ($P<0.01$) were significantly lower than the ratios before MCAO (baseline), whereas no significant difference was observed in the ratio of CCD to the unaffected sides for RBC velocity between baseline and one day after MCAO (Fig. 2).

2.2. *Longitudinal measurement in hemodynamic response to CCD*

Longitudinal LDF measurement was performed for 2 weeks (Fig. 1). Before this experiment, we confirmed that CbBF and RBC velocity and concentration in intact animals (without MCAO but with attached cranial window) were quite stable for 14 days (data not shown). The percentage changes in the ratio of the CCD side to the unaffected side for CbBF at 7 days and 14 days after MCAO were $-18\pm8\%$ and $-21\pm11\%$, respectively (Fig. 2). The percentage changes in the ratio of CCD to the unaffected sides for RBC velocity at 7 days and 14 days after MCAO were $3\pm11\%$ and $-2\pm3\%$, respectively. The percentage changes in the ratio of CCD to the unaffected sides for RBC concentration at 7 and 14 days after MCAO were $-21\pm12\%$ and $-19\pm7\%$, respectively. The ratios of CCD to the unaffected sides for CbBF and RBC concentration at 7 and 14 days after MCAO were significantly lower than those at baseline ($P<0.01$). No significant difference was observed in CbBF and RBC concentration between 7 and 14 days after MCAO. No significant difference was observed in the ratio of CCD to the unaffected sides for RBC velocity throughout all measurements (Fig. 2).

2.3. *MRI measurement in MCAO*

The high intensity area in the cerebral cortical region of the MCAO side indicates infarction in the MCA territory in the T2-weighted image two weeks after MCAO for all mice (Fig. 3).

3. Discussion

We newly developed an awake mouse model of CCD (neural deactivation) caused by MCAO. Using these CCD model mice, the hemodynamic responses to neural deactivation including

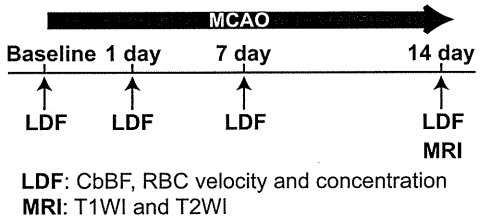

Fig. 1 – Experimental protocol for LDF measurement and MRI. LDF measurements were performed before (baseline) and 1, 7, and 14 days after MCAO. In each examination, changes in CbBF and RBC velocity and concentration were measured in both CCD side and unaffected side in awake mice. MRI experiments (T1-weighted imaging (T1WI) and T2-weighted imaging (T2WI)) were performed 14 days after MCAO.

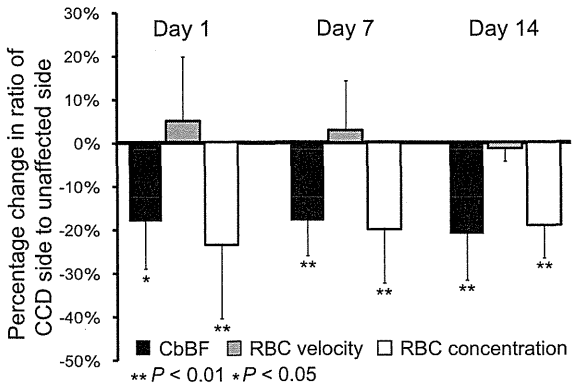

Fig. 2 – The percentage change in the ratio of CCD side to unaffected side for CbBF, RBC velocity and RBC concentration 1 day, 7 days and 14 days after CCD. Black, gray, and white bars indicate the percentage change in ratio of CCD to unaffected sides for CbBF, RBC velocity and RBC concentration, respectively. Error bars represent SD. (P<0.01 and *P<0.05).**

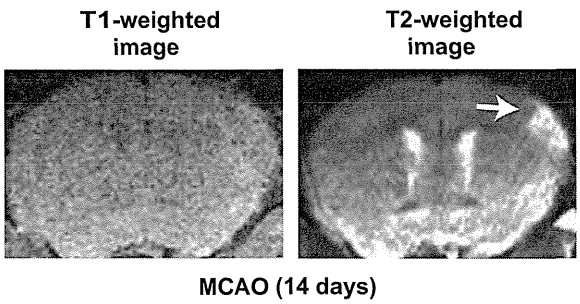

Fig. 3 – MRI experiments 14 days after MCAO. Left shows T1-weighted image. Right shows T2-weighted image. White arrow indicates the high intensity area in the T2-weighted image.

both RBC velocity and concentration were measured. This is the first observation of the effects of neural deactivation on the hemodynamics of awake mice. MRI examination showed the cerebral infarction in the unilateral cerebral cortex after MCAO (Fig. 3). The degree of decrease in CbBF caused by CCD remained almost the same throughout 2 weeks after MCAO. The reduction in RBC concentration was far greater than that in RCB velocity, suggesting that the change in RBC concentration played a dominant role in the reduction of CbBF under CCD. In human PET studies, CBF and CBV were significantly lower on the CCD side than the unaffected side, and the degree of difference between CBF of the two sides was almost the same as that between CBV. This resulted in there being no difference in vascular mean transit time (MTT), that is, the ratio of CBV to CBF, between the CCD and unaffected sides (Ito et al., 2002). This indicates that vascular blood velocity did not change during neural deactivation in the human PET study. If the RBC concentration can be considered an indicator of CBV, hemodynamic changes due to neural deactivation measured by LDF might be in good agreement with the PET measurement in humans previously reported (Ito et al., 2002).

The relationship between changes in RBC velocity and concentration due to a neural deactivation is opposite to that from a neural activation in which change in RBC velocity was seen to have a dominant role in increase in CBF (Takuwa et al., 2012). In a previous human PET study, the relationship between changes in MTT, the ratio of CBV to CBF, and CBV due to a neural deactivation (Ito et al., 2002) was opposite to that from a neural activation (Ito et al., 2005). These findings indicate the similarities between animal LDF studies and human PET studies under both neural activation and deactivation.

Our previous study confirmed that our apparatus could measure stable and reproducible CBF in awake mouse brain over a 1-week period (Takuwa et al., 2011). The present study also showed stable and reproducible CbBF, RBC velocity and concentration under CCD throughout a 2-week experimental period after MCAO. Therefore, we could conclude that the CCD model mice in this study could be used to investigate not only the mechanism of neural deactivation but also the long-term effects of CCD on neural and vascular function in brain using two-photon microscopy, animal PET and MRI.

The reason for the decrease in RBC concentration but the lack of change in RBC velocity under CCD is still unclear. According to Poiseuille's law, the flow of blood through a vessel is proportional to the fourth power of the vessel diameter; blood volume is proportional to the square of the diameter. Thus, $CBV = cCBF^{0.5}$ (c: constant; Ito et al., 2001, 2002, 2003). Based on this equation, the degree of change in CBV associated with a decrease in CBF during neural deactivation is higher than in CBV associated with an increase in CBF during neural activation. The relationship between CBF and CBV in this equation can explain the results of human PET studies in neural activation (Ito et al., 2005) and neural deactivation (Ito et al., 2002). Therefore, we previously hypothesized that hemodynamic changes in neural activation and deactivation are based on Poiseuille's law (Ito et al., 2002). The present study as well as the previous study in neural activation using LDF (Takuwa et al., 2012) shows the same tendency as those human PET studies.

Yamauchi et al. (1999a, 1999b) previously reported that CCD caused by unilateral supratentorial infarction showed a reduction of hematocrit in the CCD side of the cerebellum in a human PET study. Although we did not confirm decreased hematocrit in the CCD side in this model mouse, the reduction of RBC concentration in the CCD side might be associated with not only a decrease in CBV but also a reduction in hematocrit.

The regulatory mechanism of CbBF in the CCD side must be associated with several factors. Gold and Lauritzen (2002) showed that reduced neuronal activity in the cerebral cortex leads to a decrease in spontaneous Purkinje cell spike activity in the contralateral cerebellar hemisphere using anesthetized CCD model rat. It is possible that the attenuation of spontaneous neural activation in cerebellum caused a decrease in synthetase of a vasoactive mediator in neurovascular coupling (e.g., nitric oxide (NO), cyclooxygenase-2 (Cox-2) and adenosine) released from neurons and glia by neural activity (Yang et al., 2003; Bakalova et al., 2002; Ko et al., 1990). To explore the mechanism, further experiments using synthetase inhibitors or immunostaining techniques in mice will be

needed. On the other hand, Garbuzova-Davis et al. (2013) reported that microvascular damage (blood–brain barrier (BBB) impairment) was caused after MCAO not only ipsilateral cerebral hemisphere but also contralateral cerebral hemisphere in ischemic stroke rat model. Since neuronal deactivation in this CCD model mice was associated with the cerebral infarction, investigation of microvascular damage (for example, BBB impairment) in CCD side of cerebellum might be needed.

Although hemodynamic change in neural deactivation were measured 1 day, 7 days, and 14 days after MCAO, the acute phase just after the MCAO must show ideal deactivation condition. However, LDF measurement immediately after MCAO could not be performed because animal condition just after surgical procedure is not suitable for LDF experiments with awake condition.

Although Gold and Lauritzen (2002) showed that reduced neuronal activity evaluated by Purkinje cell field potentials in the cerebellar cortex after MCAO, the reduction of neuronal activity in cerebellum after MCAO in the CCD model mice was not confirmed in the present study. To validate the neural deactivation under CCD, measurements of neural activation (for example, voltage sensitive dye imaging) before and after MCAO will be needed as a further study.

In conclusion, we developed CCD model mice and found that the relation between RBC velocity and concentration during neural deactivation was similar to that shown in humans using PET. Moreover, longitudinal experiments showed a stable and reproducible response of CbBF, RBC velocity and concentration induced by CCD in awake mice. It is likely that our newly established mouse model of CCD will be useful for investigation of the effects of neural deactivation on cerebral hemodynamics and pathophysiology using two-photon laser microscopy and animal PET.

4. Experimental procedures

4.1. *Animal preparation*

All experiments were performed in accordance with the institutional guidelines on humane care and use of laboratory animals and were approved by the Institutional Committee for Animal Experimentation. Six male C57BL/6J mice (20–30 g, 7–11 weeks; Japan SLC, Inc., Hamamatsu, Japan) were used in two experiments: LDF measurements and MRI measurement (Fig. 1). The animals were housed in a 12-h light/dark cycle room at a temperature of 25 °C with ad libitum water and food.

For the surgical procedure, the animals were anesthetized with a mixture of air, oxygen and isoflurane (3% for induction and 2% for surgery) via facemask. The animals were fixed in a stereotactic frame, and rectal temperature was maintained at 37.0 °C using a heating pad (ATC-210, Unique Medical Co. Ltd., Tokyo, Japan). The methods for preparing the chronic cranial window have been reported in detail by Tomita et al. (2005) and Takuwa et al. (2013). A midline incision (10 mm) was made to expose the skull. Two cranial windows (2–3 mm diameter) were attached over the left and right side of the cerebellar cortex (coordinates: 1 mm posterior from the occipital bone, 4 mm lateral), keeping the dura intact. A custom metal plate was affixed to the front of the skull using dental cement (Ionosit, DMG, Hamburg, Germany). After completion of the surgery, the animals were allowed to recover from anesthesia and housed for at least 7 days before initiation of the experiments.

In this experiment, MCAO was performed in six animals by Tamura et al. (1981) method. Briefly, permanent occlusion was made at the proximal branch of the MCA in the left cerebral cortex. Thus, the right and left sides of the cerebellar cortex were defined as CCD side and unaffected side, respectively.

4.2. *Experimental protocols*

The experimental protocol for LDF measurements in awake mice was reported previously (Takuwa et al., 2011). Briefly, the metal plate on the animal's head was screwed to a custom-made stereotactic apparatus. The animal was then placed on a styrofoam ball that was floating using a stream of air. This allowed the animal to exercise freely on the ball while the animal's head was fixed to the apparatus. LDF measurements were repeatedly performed in both the CCD side and the unaffected side of the cerebellar cortex before (baseline) 1 day, 7 days, and 14 days after MCAO (Fig. 1).

4.3. *CbBF and RBC velocity and concentration measurements*

CbBF, RBC velocity and concentration were measured with an LDF system (FLO-C1, OMEGAWAVE, Tokyo, Japan) using an LDF probe with a 0.46-mm tip diameter (Probe NS; OMEGAWAVE) placed perpendicular to the cerebellar cortex through a guide tube. The guide tube was attached to the cranial windows using dental cement (Ionosit, DMG, Hamburg, Germany), avoiding areas with large blood vessels (Matsuura and Kanno, 2001). Our LDF system simultaneously provides three parameters: flux (CBF), RBC concentration and RBC velocity, where RBC velocity=CBF/RBC concentration (Nilsson, 1984). The volume of LDF measurement was approximately 1 mm^3 (Nilsson et al., 1980). A sampling rate of 0.1 s was used for measuring all LDF signals (CbBF, RBC velocity and concentration). CbBF and RBC velocity and concentration recordings were obtained during 30 min in every experiment.

4.4. *Data analysis*

During the experiments, LDF data were recorded using a polygraph data acquisition system (MP150; BIOPAC Systems, Inc., Goleta, CA, USA) and analyzed offline. At first, the values of CBF, RBC velocity and concentration were averaged for 30 min. The hemodynamic change in the CCD side of the cerebellum was evaluated by the ratio of the CCD side to the unaffected side in the cerebellum. The ratio is expressed as follows:

$$A = B/C,$$

where A is the ratio of the CCD side to the unaffected side, B is the averaged LDF parameters (CbBF and RBC velocity and concentration) in the CCD side, and C is the averaged LDF parameters in the unaffected side. The ratio of CCD side to

unaffected side was calculated on all measurement days. These parameters were statistically analyzed by paired t-test. The percentage change in the ratio of the CCD side to the unaffected side was calculated as follows:

$$\%\text{Change} = A_{MCAO}/A_{Baseline} - 1 \times 100,$$

where $A_{Baseline}$ is A at baseline and A_{MCAO} is A after MCAO.

4.5. *MRI experiments*

All MRI experiments were performed on a 7.0T horizontal MRI scanner (Magnet: Kobelco and JASTEC, Japan; Console: Bruker Biospin, Germany) with a volume coil for transmission (Bruker Biospin) and a 2-ch phased array surface coil for reception (Rapid Biomedical, Germany). The mice were initially anesthetized with 3.0% isoflurane (Escain, Mylan Japan, Japan), and then anesthetized with 1.5~2.0% isoflurane and 1:5 oxygen/room-air-mixture during the MRI experiments. Rectal temperature was continuously monitored using an optical fiber thermometer (FOT-M, FISO, Canada) and maintained at 36.5±0.5 °C using a heating pad (Rapid Biomedical) and warm air. The surface coil was placed under the chin of the prone mice because the guide tubes of the LDF probes were attached over the cranial window (cerebellar cortex). The first imaging slices were carefully set at the rhinal fissure with reference to the mouse brain atlas (Paxinos and Franklin, 2004). Each image set consisted of two different kinds of MRI measurements performed in the following order: T1-weighted and T2-weighted MR images at two weeks after MCAO.

T1-weighted MRI: Transaxial T1-weighted MR images were acquired using a multi-slice spin echo sequence. The imaging parameters were as follows: repetition time (TR)/echo time (TE)=400/9.6 ms, slice thickness=1.0 mm, slice gap=0.0 mm, fat-sup=off, matrix=256 × 256, field of view (FOV)=25.6 × 25.6 mm^2, number of averages (NA)=4, number of slices=13, and scan time=6 min 49 s.

T2-weighted MRI: Transaxial T2-weighted fast spin-echo MR images were acquired using a rapid acquisition with relaxation enhancement (RARE) sequence in the same slice position as the T1-weighted MRI. The imaging parameters were as follows: TR/effective TE=4200/36 ms, Fat-Sup=on, NA=4, RARE factor=8, number of slices=13, and scan time=6 min 43 s. Frequency selective saturation pulses and crusher magnetic field gradients were used for fat suppression.

Role of funding source

There are no roles of sponsors in the conduct of the research or preparation of the article.

Contributors

H.T. and H.I. designed the research; H.T. and Y.T. performed the research; H.T., Y.T. and D.K. analyzed the data; Y.T., D.K., I.A., H.K., Y.I., J.T., T.M., K.M., C.S., N.S. and I.K. helped with the data interpretation and discussion; H.T. and H.I. wrote the paper.

Acknowledgments

The assistance of members of the National Institute of Radiological Sciences in performing the LDF experiments is gratefully acknowledged. This work was partially supported by a Grant-in-Aid for Scientific Research to T. M. from the Japan Society for the Promotion of Science. The authors thank Sayaka Shibata, Aiko Sekita and Nobuhiro Nitta for the MRI experiments.

REFERENCES

Bakalova, R., Matsuura, T., Kanno, I., 2002. The cyclooxygenase inhibitors indomethacin and rofecoxib reduce regional cerebral blood flow evoked by somatosensory stimulation in rats. Exp. Biol. Med 227, 465–473.

Garbuzova-Davis, S., Rodrigues, M.C., Hernandez-Ontiveros, D.G., Tajiri, N., Frisina-Deyo, A., Boffeli, S.M., Abraham, J.V., Pabon, M., Wagner, A., Ishikawa, H., Shinozuka, K., Haller, E., Sanberg, P.R., Kaneko, Y., Borlongan, C.V., 2013. Blood-brain barrier alterations provide evidence of subacute diaschisis in an ischemic stroke rat model. PLoS One 8 (5), e63553 (10).

Gold, L., Lauritzen, M., 2002. Neuronal deactivation explains decreased cerebellar blood flow in response to focal cerebral ischemia or suppressed neocortical function. Proc. Nat. Acad. Sci. U.S.A 99, 7699–7704.

Ito, H., Takahashi, K., Hatazawa, J., Kim, S.G., Kanno, I., 2001. Changes in human regional cerebral blood flow and cerebral blood volume during visual stimulation measured by positron emission tomography. J. Cereb. Blood Flow Metab 21, 608–612.

Ito, H., Kanno, I., Shimosegawa, E., Tamura, H., Okane, K., Hatazawa, J., 2002. Hemodynamic changes during neural deactivation in human brain: a positron emission tomography study of crossed cerebellar diaschisis. Ann. Nucl. Med 16, 249–254.

Ito, H., Kanno, I., Ibaraki, M., Hatazawa, J., Miura, S., 2003. Changes in human cerebral blood flow and cerebral blood volume during hypercapnia and hypocapnia measured by positron emission tomography. J. Cereb. Blood Flow Metab 23, 665–670.

Ito, H., Ibaraki, M., Kanno, I., Fukuda, H., Miura, S., 2005. Changes in cerebral blood flow and cerebral oxygen metabolism during neural activation measured by positron emission tomography: comparison with blood oxygenation level-dependent contrast measured by functional magnetic resonance imaging. J. Cereb. Blood Flow Metab 25, 371–377.

Ko, K.R., Ngai, A.C., Winn, R.H., 1990. Role of adenosine in regulation of regional cerebral blood flow in sensory cortex. Am. J. Physiol 259, 1703–1708.

Lahti, K.M., Ferris, C.F., Li, F., Sotak, C.H., King, J.A., 1999. Comparison of evoked cortical activity in conscious and propofol-anesthetized rats using functional MRI. Magn. Reson. Med. 41, 412–416.

Lenzi, G.L., Frackowiak, R.S., Jones, T., 1982. Cerebral oxygen metabolism and blood flow in human cerebral ischemic infarction. J. Cereb. Blood Flow Metab 2, 321–335.

Martin, C., Berwick, J., Johnston, D., Zheng, Y., Martindale, J., Port, M., Redgrave, P., Mayhew, J., 2002. Optical imaging spectroscopy in the unanaesthetised rat. J. Neurosci. Methods 120, 25–34.

Martin, C., Martindale, J., Berwick, J., Mayhew, J., 2006. Investigating neural-hemodynamic coupling and the hemodynamic response function in the awake rat. NeuroImage 32, 33–48.

Martin, W.R., Raichle, M.E., 1983. Cerebellar blood flow and metabolism in cerebral hemisphere infarction. Ann. Neurol 14, 168–176.

Matsuura, T., Kanno, I., 2001. Changes in red blood cell behavior during cerebral blood flow increase in the rat somatosensory cortex: a study of laser-Doppler flowmetry. Jpn. J. Physiol 51, 703–708.

Nilsson, G.E., 1984. Signal processor for laser Doppler tissue flowmeters. Med. Biol. Eng. Comput. 22, 343–348.

Nilsson, G.E., Tenland, T., Öberg, P.A., 1980. Evaluation of a laser Doppler flowmeter for measurement of tissue blood flow. IEEE Trans. Biomed. Eng. BME-27, 597–604.

Pantano, P., Baron, J.C., Samson, Y., Bousser, M.G., Derouesne, C., Comar, D., 1986. Crossed cerebellar diaschisis. Further studies. Brain 109, 677–694.

Paxinos, G., Franklin, K.B.J., 2004. The Mouse Brain in Stereotaxic Coordinates. Gulf Professional Publishing.

Peeters, R.R., Tindemans, I., De Schutter, E., Van der Linden, A., 2001. Comparing BOLD fMRI signal changes in the awake and anesthetized rat during electrical forepaw stimulation. Magn. Reson. Imaging 19, 821–826.

Sicard, K., Shen, Q., Brevard, M.E., Sullivan, R., Ferris, C.F., King, J.A., Duong, T.Q., 2003. Regional cerebral blood flow and BOLD responses in conscious and anesthetized rats under basal and hypercapnic conditions: implications for functional MRI studies. J. Cereb. Blood Flow Metab 23, 472–481.

Takuwa, H., Autio, J., Nakayama, H., Matsuura, T., Obata, T., Okada, E., Masamoto, K., Kanno, I., 2011. Reproducibility and variance of a stimulation-induced hemodynamic response in barrel cortex of awake behaving mice. Brain Res 1369, 103–111.

Takuwa, H., Matsuura, T., Obata, T., Kawaguchi, H., Kanno, I., Ito, H., 2012. Hemodynamic changes during somatosensory stimulation in awake and isoflurane-anesthetized mice measured by laser-Doppler flowmetry. Brain Res 1472, 107–112.

Takuwa, H., Masamoto, K., Yamazaki, K., Kawaguchi, H., Ikoma, Y., Tajima, Y., Obata, T., Tomita, Y., Suzuki, N., Kanno, I., Ito, H., 2013. Long-term adaptation of cerebral hemodynamic response to somatosensory stimulation during chronic hypoxia in awake mice. J. Cereb. Blood Flow Metab 33, 774–779.

Tamura, A., Graham, D.I., McCulloch, J., Teasdale, G.M., 1981. Focal cerebral ischaemia in the rat: 1. Description of technique and early neuropathological consequences following middle cerebral artery occlusion. J. Cereb. Blood Flow Metab 1, 53–60.

Tomita, Y., Kubis, N., Calando, Y., Tran Dinh, A., Meric, P., Seylaz, J., Pinard, E., 2005. Long-term in vivo investigation of mouse cerebral microcirculation by fluorescence confocal microscopy in the area of focal ischemia. J. Cereb. Blood Flow Metab. 25, 858–867.

Yamauchi, H., Fukuyama, H., Kimura, J., 1992a. Hemodynamic and metabolic changes in crossed cerebellar hypoperfusion. Stroke 23, 855–860.

Yamauchi, H., Fukuyama, H., Yamaguchi, S., Doi, T., Ogawa, M., Ouchi, Y., Kimura, J., Sadatoh, N., Yonekura, Y., Tamaki, N., Konishi, J., 1992b. Crossed cerebellar hypoperfusion in unilateral major cerebral artery occlusive disorders. J. Nucl. Med 33, 1632–1636.

Yamauchi, H., Fukuyama, H., Nagahama, Y., Nishizawa, S., Konishi, J., 1999a. Uncoupling of oxygen and glucose metabolism in persistent crossed cerebellar diaschisis. Stroke 30, 1424–1428.

Yamauchi, H., Fukuyama, H., Nagahama, Y., Okazawa, H., Konishi, J., 1999b. A decrease in regional cerebral blood volume and hematocrit in crossed cerebellar diaschisis. Stroke 30, 1429–1431.

Yang, G., Zhang, Y., Ross, M.E., Iadecola, C., 2003. Attenuation of activity-induced increases in cerebellar blood flow in mice lacking neuronal nitric oxide synthase. Am. J. Physiol. Heart Circ. Physiol 285, 298–304.

Neuron
Article

Imaging of Tau Pathology in a Tauopathy Mouse Model and in Alzheimer Patients Compared to Normal Controls

Masahiro Maruyama,[1,10] Hitoshi Shimada,[1,10] Tetsuya Suhara,[1] Hitoshi Shinotoh,[1] Bin Ji,[1] Jun Maeda,[1] Ming-Rong Zhang,[1] John Q. Trojanowski,[2] Virginia M.-Y. Lee,[2] Maiko Ono,[1] Kazuto Masamoto,[1] Harumasa Takano,[1] Naruhiko Sahara,[3,5,6] Nobuhisa Iwata,[4] Nobuyuki Okamura,[7] Shozo Furumoto,[7] Yukitsuka Kudo,[8] Qing Chang,[9] Takaomi C. Saido,[4] Akihiko Takashima,[3] Jada Lewis,[5,6] Ming-Kuei Jang,[9] Ichio Aoki,[1] Hiroshi Ito,[1] and Makoto Higuchi[1,*]
[1]Molecular Imaging Center, National Institute of Radiological Sciences, 4-9-1 Anagawa, Inage-ku, Chiba, Chiba 263-8555, Japan
[2]Center for Neurodegenerative Disease Research, University of Pennsylvania Perelman School of Medicine, Third Floor HUP-Maloney, 36th and Spruce Streets, Philadelphia, PA 19104, USA
[3]Laboratory for Alzheimer's Disease
[4]Laboratory for Proteolytic Neuroscience
RIKEN Brain Science Institute, 2-1 Hirosawa, Wako, Saitama 351-0198, Japan
[5]Center for Translational Research in Neurodegenerative Disease
[6]Department of Neuroscience
University of Florida, 1275 Center Drive, Gainesville, FL 32610, USA
[7]Department of Pharmacology, Tohoku University Graduate School of Medicine, 2-1 Seiryo-machi, Aoba-ku, Sendai, Miyagi 980-8575, Japan
[8]Clinical Research, Innovation and Education Center, Tohoku University Hospital, 1-1 Seiryo-machi, Aoba-ku, Sendai, Miyagi 980-8574, Japan
[9]Institute for Applied Cancer Science, MD Anderson Cancer Center, 1901 East Road, Houston, TX 77054, USA
[10]These authors contributed equally to this work
*Correspondence: mhiguchi@nirs.go.jp
http://dx.doi.org/10.1016/j.neuron.2013.07.037

SUMMARY

Accumulation of intracellular tau fibrils has been the focus of research on the mechanisms of neurodegeneration in Alzheimer's disease (AD) and related tauopathies. Here, we have developed a class of tau ligands, phenyl/pyridinyl-butadienyl-benzothiazoles/benzothiazoliums (PBBs), for visualizing diverse tau inclusions in brains of living patients with AD or non-AD tauopathies and animal models of these disorders. In vivo optical and positron emission tomographic (PET) imaging of a transgenic mouse model demonstrated sensitive detection of tau inclusions by PBBs. A pyridinated PBB, [^{11}C]PBB3, was next applied in a clinical PET study, and its robust signal in the AD hippocampus wherein tau pathology is enriched contrasted strikingly with that of a senile plaque radioligand, [^{11}C]Pittsburgh Compound-B ([^{11}C]PIB). [^{11}C]PBB3-PET data were also consistent with the spreading of tau pathology with AD progression. Furthermore, increased [^{11}C]PBB3 signals were found in a corticobasal syndrome patient negative for [^{11}C]PIB-PET.

INTRODUCTION

Hallmark pathologies of Alzheimer's disease (AD) are extracellular senile plaques consisting of aggregated amyloid β peptide (Aβ) and intraneuronal neurofibrillary tangles (NFTs) composed of pathological tau fibrils, while similar tau lesions in neurons and glia are also characteristic of other neurodegenerative disorders, such as progressive supranuclear palsy (PSP) and corticobasal degeneration (CBD), that are collectively referred to as tauopathies (Ballatore et al., 2007). The discovery of *tau* gene mutations in a familial form of tauopathy, known as frontotemporal dementia and parkinsonism linked to chromosome 17 (FTDP-17), and subsequent studies of transgenic (Tg) mice expressing human tau with or without these mutations, clearly implicate pathological tau in mechanisms of neurodegeneration in AD and related tauopathies (Ballatore et al., 2007). Thus, there is an urgent need for tau imaging techniques to complement Aβ amyloid imaging methods that now are widely used.

In vivo imaging modalities, as exemplified by positron emission tomography (PET) (Klunk et al., 2004; Small et al., 2006; Kudo et al., 2007; Maeda et al., 2007), optical scanning (Bacskai et al., 2003; Hintersteiner et al., 2005), and magnetic resonance imaging (MRI) (Higuchi et al., 2005), have enabled visualization of Aβ deposits in humans with AD and/or AD mouse models, and there has been a growing expectation that low-molecular-weight ligands for β-pleated sheet structures will also serve as molecular probes for tau amyloids. Although the majority of plaque-imaging agents used for clinical PET studies do not bind to tau lesions (Klunk et al., 2003), at least one radiolabeled β sheet ligand, [^{18}F]FDDNP, enables PET imaging of AD NFTs (Small et al., 2006). However, a relatively low contrast of in vitro autoradiographic and in vivo PET signals for [^{18}F]FDDNP putatively reflecting tau lesions does not allow a simple visual inspection of images for the assessment of tau pathologies in living subjects

(Small et al., 2006; Thompson et al., 2009). Thus, better tau radioligands with higher affinity for tau fibrils and/or less nonspecific binding to tissues are urgently needed to complement high-contrast senile plaque imaging agents, including widely studied [^{11}C]Pittsburgh Compound-B ([^{11}C]PIB) (Klunk et al., 2004) and United States Food and Drug Administration-approved [^{18}F]florbetapir (Yang et al., 2012). In addition, [^{18}F]FDDNP and several other candidate tau probes do not bind to tau inclusions in non-AD tauopathy brains without plaque deposition (Okamura et al., 2005) and therefore can be clinically characterized only in AD patients with comingled Aβ and tau amyloids. Hence, compounds that detect diverse tau aggregates, including tau inclusions in non-AD neurodegenerative diseases and tau Tg models, could be used to interrogate in vivo interactions between exogenous ligands and tau pathologies.

Here, we found that the lipophilicity of β sheet ligands is associated with their selectivity for tau versus Aβ fibrils and that the core dimensions of these chemicals are major determinants of their reactivity with a broad spectrum of tau aggregates in diverse tauopathies and mouse models of tau pathology. Building on these observations, we developed a series of fluorescent compounds capable of detecting diverse tau lesions using optical and PET imaging in living Tg mouse models of tauopathies. Finally, we identified a radiotracer that produced the highest contrast for tau inclusions in animal PET and used it in exploratory in vivo imaging studies of AD patients, providing clear demonstration of signal intensification in tau-rich regions, in sharp distinction to [^{11}C]PIB-PET data reflecting plaque deposition.

RESULTS

Identification of PBBs as Ligands for Diverse Tau Inclusions in Human Tauopathies

We screened an array of fluorescent chemicals capable of binding to β sheet conformations (see the Compounds subsection in the Experimental Procedures). Fluorescence labeling with these compounds were examined in sections of AD brains bearing Aβ and tau amyloids (Figures 1A and 2A) and non-AD tauopathy brains characterized by tau inclusions and few or no Aβ plaques (Figure 2). Amyloid PET tracers currently used for human PET studies, PIB (Klunk et al., 2004), and BF-227 (Kudo et al., 2007), tightly bound to senile plaques, while they only weakly reacted with AD NFTs (Figures 1A; Figure S1 available online). PET probes reported to selectively label tau aggregates, BF-158 (Okamura et al., 2005) and THK523 (Fodero-Tavoletti et al., 2011), detected AD NFTs (Figures 2A and S1) but microscopically detectable fluorescence signals produced by FDDNP, which are presumed to bind to both Aβ and tau fibrils (Small et al., 2006), were consistent with dense cores of classic plaques and distinct from tau lesions (Figures 2A and S1). None of the above-mentioned PET ligands were reactive with tau inclusions in non-AD tauopathies, such as Pick bodies in Pick's disease (Figures 2A and S1) and neuronal and glial fibrillary lesions in PSP and CBD (data not shown). By contrast, these pathologies were intensely labeled with a widely used amyloid dye, thioflavin-S, and a derivative of another classic amyloid dye Congo red, (E,E)-1-fluoro-2,5-bis(3-hydroxycarbonyl-4-hydroxy)styrylbenzene (FSB) (Higuchi et al., 2005; Maeda et al., 2007) (Figures 1, 2A, and S1), although these chemicals may not undergo efficient transfer through the blood-brain barrier (BBB) (Zhuang et al., 2001). Because compounds possessing a π-electron-conjugated backbone longer than 13Å exhibited affinities for pathological inclusions in a broad range of tauopathies, we examined binding of additional chemicals with a variety of structural dimensions to tau aggregates and found that affinity for non-AD tau inclusions could be attributed to a core structure with a specific extent ranging from 13 to 19 Å (Figure S1). Based on this view and the known fact that chemicals with a flat and slender backbone could pass through and attach to channel-like accesses in β-pleated sheets (Krebs et al., 2005), we developed a class of compounds, phenyl/pyridinyl-butadienyl-benzothiazoles/benzothiazoliums (PBBs), by stretching the core structure of a prototypical fluorescent amyloid dye, thioflavin-T, with two C = C double bond inserts between aniline (or aminopyridine) and benzothiazole (or benzothiazolium) groups (Figure 1B).

All PBB compounds intensely labeled NFTs, neuropil threads, and plaque neurites in AD brains (Figure 1C). Interestingly, the affinity of these PBBs for Aβ plaques lacking dense cores was positively correlated with their lipophilicity (Figure 1C), and thereby three potential probes with relatively low logP (log of the octanol/water partition coefficient) values, including PBB3, 2-[4-(4-methylaminophenyl)-1,3-butadienyl]-benzothiazol-5,6-diol (PBB4) and PBB5 (structurally identical to Styryl 7, CAS registry number 114720-33-1), appeared suitable for visualizing tau pathologies in living organisms with reasonable selectivity. High-affinity of PBBs for tau lesions was further demonstrated by fluorometric analyses using Aβ and tau filaments assembled in a test tube (Table S1; experimental procedures are given in the Supplemental Experimental Procedures), but the most and least lipophilic PBB members displayed similar selectivity for in vitro tau versus Aβ pathologies, implying a methodological limitation in screening chemicals for tau-selective ligands based on binding to synthetic peptides and recombinant proteins. PBBs and FSB were also shown to label tau inclusions in non-AD tauopathies, such as Pick's disease (Figures 2A and S1), PSP, and CBD (Figure 2B), all of which were immunodetected by an antibody specific for phosphorylated tau proteins (AT8).

In Vitro and Ex Vivo Fluorescence Imaging of Tau Lesions in Tau Tg Mice by PBBs

To obtain in vivo evidence of direct interaction between PBBs and tau lesions, we employed Tg mice expressing a single human four-repeat tau isoform with the P301S FTDP-17 mutation (PS19 line, see Figure S2 for neuropathological features of this Tg strain) (Yoshiyama et al., 2007). Similar to the findings in non-AD tauopathy brains, NFT-like inclusions in the brain stem and spinal cord of PS19 mice were clearly recognized by PBBs (Figures 3A and S1). We then performed ex vivo fluorescence labeling of tau lesions in PS19 mice with intravenously administered PBBs. Brains and spinal cords were removed 60 min after tracer injection, and fluorescence microscopy revealed an intense accumulation of these compounds in fibrillary tau inclusions abundantly seen throughout the sections by

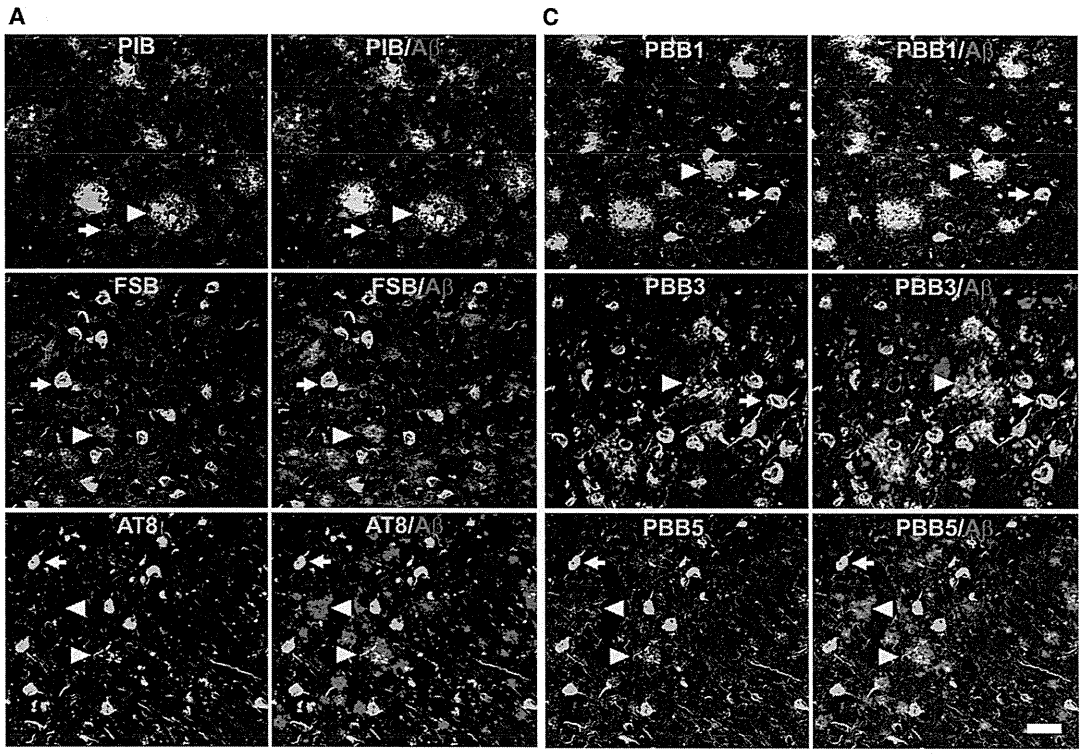

B

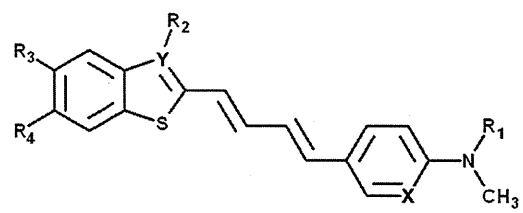

Compound	R_1	R_2	R_3	R_4	X	Y	ClogP
PBB1	CH_3	-	H	H	C(H)	N	5.44
PBB2	H	-	H	OH	C(H)	N	3.57
PBB3	H	-	H	OH	N	N	3.30
PBB4	H	-	OH	OH	C(H)	N	2.97
PBB5	CH_3	CH_3CH_2	H	H	C(H)	N^+	2.32

Figure 1. Design and Characterization of PBB Compounds as Potential Imaging Agents for Tauopathies

(A) Confocal fluorescence images of frontal cortex sections from an AD patient. Following fluorescence labeling (pseudocolors are converted to green) with PIB (top row) and FSB (middle row), the samples were immunostained with an antibody against AβN3(pE) (red in the right column). PIB intensely labeled Aβ plaques (white arrowheads) but did not clearly label NFTs (arrows). By contrast, NFTs and neuropil threads were intensely labeled by FSB, whereas the staining of diffuse plaques was negligible. A section was also doubly immunolabeled (bottom row) with AT8 (green) and anti-AβN3(pE) antibodies (red in the right panel), to demonstrate the abundance of tau and Aβ amyloids in this area. Yellow arrowheads indicate tau-positive dystrophic neurites associated with senile plaques.

(B) Structures of PBBs. Neutral benzothiazoles (PBB1-4) are newly synthesized chemicals, and a charged benzothiazolium, PBB5, is identical to a commercially available near-infrared laser dye.

(C) Confocal fluorescence images of PBBs (pseudocolors are converted to green) and AβN3(pE) (red in the right column) staining in sections adjacent to those displayed in (A). The intensity of plaque staining (arrowheads) relative to that of NFTs (arrows) was positively associated with the lipophilicity of PBBs. As compared with PBB1 (top row) staining, labeling of diffuse plaques with PBB3 (middle row) was substantially attenuated. PBB5 was nearly unreactive with diffuse plaques (bottom row), and subsequent double immunofluorescence staining of the same section (bottom row in C) illustrated good agreement of PBB5 labeling with the distribution of AT8-positive NFTs.

Scale bar, 50 μm (A and C). See also Figure S1 and Table S1.

staining with thioflavin-S, FSB, and AT8 (Figure 3B). On the other hand, no overt in vitro (Figure 3A) or ex vivo (data not shown) fluorescence of these ligands was noted in the corresponding regions of non-Tg wild-type (WT) mice. Consistent with these observations, two-photon laser scanning fluorescence microscopy of ex vivo samples demonstrated somatic and neuritic staining of a subset of tangle-bearing neurons with intravenously injected 2-[4-(4-methylaminophenyl)-1,3-butadienyl]-benzothiazol-6-ol (PBB2) and PBB4 in unsliced spinal cord blocks from PS19 mice (Figure 3B).

In Vivo Macroscopic and Mesoscopic Optical Detection of Fibrillar Tau Pathologies in a Mouse Model Using PBB5

We next characterized PBBs with the use of in vivo fluorescence imaging modalities, which permitted a quick assessment of

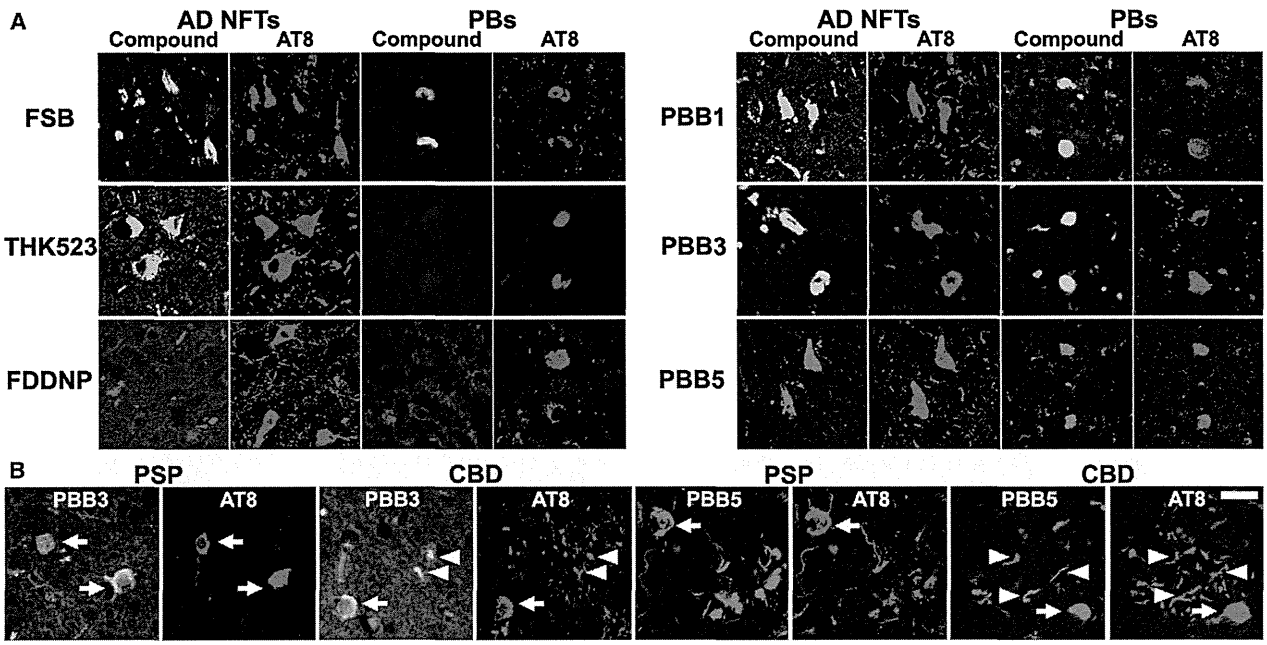

Figure 2. Binding of Tau Ligands to Tau Lesions in AD and Non-AD Tauopathy Brains

(A) Double fluorescence staining of AD NFTs and Pick bodies (PBs) in Pick's disease with PBBs, other tau ligands, and anti-phospho-tau antibody (AT8). FSB and PBBs sensitively captured AD NFTs and PBs. AD NFTs were labeled with THK523. Meanwhile, PBs were not visualized by these compounds. NFTs and PBs were barely recognizable by using FDDNP.

(B) Double fluorescence staining of neuronal tau inclusions (arrows) in PSP and CBD and putative astrocytic plaques (arrowheads) in CBD. A substantial portion of tau fibrils in neurons were captured by PBB3 and PBB5, but a much smaller subset of phosphorylated tau aggregates in astrocytic plaques were labeled with these compounds.

Scale bar, 20 μm (A and B). See also Figures S2 and S3.

candidate chemicals without the need for radiolabeling. Because PBB5 is fluorescent, with peak excitation and emission wavelengths in a near-infrared range (Table S1), this compound is applicable to in vivo optical imaging of tau deposits in laboratory animals. To examine this possibility, fluorescence images were obtained from living mice over a time course following intravenous PBB5 injections using a small animal-dedicated system permitting the intravital observation of fluorescence signals at magnifications varying between macroscopic and microscopic levels. Tail vein administration of PBB5 in PS19 mice revealed strong fluorescence relative to non-Tg WT mice in the central nervous system (CNS) above the slit between the base of the skull and first vertebra, through the skin and connective tissues overlaying the cisterna magna (Figures S3A–S3D), suggesting a concentration of this tracer in the PS19 spinal cord. In line with this in vivo observation, the hindbrain and spinal cord of PS19 mice, which were dissected out at 2 hr after the injection of PBB5, exhibited increased retention of this compound compared to non-Tg WT mice (Figures S3E–S3G).

In vivo optical imaging of tau Tg mice was subsequently performed using a device equipped with a pulsed diode laser and a photomultiplier tube to detect deep signals through the skull. Elevated levels of fluorescence intensity were found in homogenized brain stem samples collected from PS19 mice at 20 hr after the intravenous tracer administration (Figure S4A), indicating a long-lasting in vivo binding of PBB5 to tau fibrils. To support the ex vivo evidence, fluorescence intensity was noninvasively analyzed in living PS19 and non-Tg WT mice treated with PBB5. The mice, with their heads shaved in advance, were prescanned, and autofluorescence signals were detected at a relatively high level in an area corresponding to the frontal forebrain. Using these baseline signals as landmarks, regions of interest (ROIs) were defined in the frontal cortex, brain stem, and spinal cord (Figure 4A). The near-infrared fluorescence was notably increased immediately after the intravenous injection of PBB5 (Figure S4C), and the fluorescence in the brain stem and spinal cord ROIs of PS19 mice much exceeded that in WT mice at 30 min (Figure 4B). Fluorescence intensity in the frontal cortex ROI, normalized on the basis of integration time and laser power, was lower in PS19 mice than in WT mice over 120 min after tracer injection (Figure S4B), which may reflect impaired CNS delivery of the tracer in Tg mice due to degenerative changes (see Figures S4C–S4L for details), and thereafter this became almost equivalent between the two genotypes (Figure S4B). Meanwhile, persistent retention of the signals in the brain stem and spinal cord ROIs of PS19 mice was observed beyond 240 min (Figures 4B and S4B). A more quantitative index comparable among different mice was determined by calculating the target-to-frontal-cortex ratio of fluorescence intensity and was shown to increase over time particularly in PS19 mice (Figures 4C and 4D). This ratio was significantly greater in PS19 mice than in WT mice at 240 min (Figure 4E), beyond which the difference

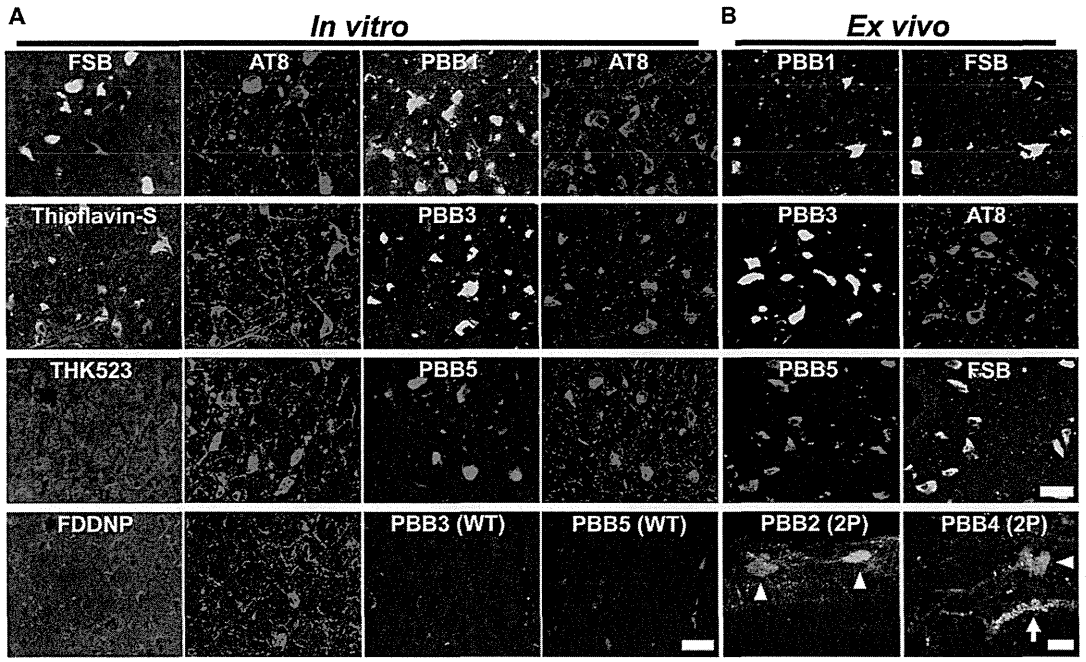

Figure 3. In Vitro and Ex Vivo Labeling of NFTs in PS19 Mice with PBB Compounds

(A) Double fluorescence staining of intraneuronal tau aggregates in postmortem brain stem slices of a 12-month-old PS19 mouse with PBB, other amyloid ligands, and anti-phospho-tau antibody (AT8).

(B) Binding of intravenously administered PBBs (0.1 mg/kg PBB5 and 1 mg/kg PBB1 and PBB3) to NFTs in PS19 mice at 10–12 months of age. The tissues were sampled at 60 min after tracer administration. The brain stem (top row) and spinal cord (second and third rows from the top) sections abundantly contained neurons showing strong fluorescence (left), and subsequent staining with FSB or AT8 (right) indicated that these cells were laden with tau amyloid fibrils (right). Putative intraneuronal tau inclusions in unsectioned spinal cords (arrowheads in the bottom row) removed from PS19 mice at 60 min after intravenous injection of PBB2 and PBB4 were also clearly visible by using a two-photon (2P) fluorescence microscopic system. Arrow in the bottom row indicates a cluster of autofluorescence signals from blood cells.

Scale bars, 25 μm (A), 30 μm (top to third rows in B), and 20 μm (bottom row in B).

between the two lines of mice became nearly constant (Figures 4C and 4D). The intensity ratio of the spinal cord ROI to the frontal cortex in PS19 mice at 240 min was also significantly correlated with the abundance of NFTs stained with FSB (Figure 4F), but such correlations were not statistically significant in the brain stem (Figure 4F), implying limitations of the intensitometry in some brain regions below the cerebellum and fourth ventricle.

Intravital Imaging of Individual Tau Inclusions by PBB3 and Two-Photon Laser Scanning Fluorescence Microscopy

Two-photon excitation microscopy, which enables optical sectioning, potentially up to 1 mm deep, in living tissues, could be utilized to visually demonstrate transfer of a fluorescent probe from the plasma compartment into the cytoplasm of CNS neurons and binding of the probe to intraneuronal tau inclusions. We therefore captured fluorescence signals from intravenously administered PBB3 by in vivo two-photon laser scanning microscopic imaging of the spinal cord of laminectomized PS19 mice. Within 3 s of PBB3 injection, green fluorescence signals emerged in blood vessels prelabeled with red with intraperitoneal treatment using sulforhodamine 101 and subsequently diffused from the vasculatures to the spinal cord parenchyma over the next few minutes (Figures 5A–5F). These diffuse signals declined thereafter due to the clearance of PBB3 from the tissue, whereas intense labeling of putative tau inclusions with green fluorescence appeared in a subpopulation of large cells morphologically identified as neurons at 3–5 min after PBB3 injection (Figures 5G and 5H). These intracellular PBB3 fluorescent signals were not found in the spinal cord of WT mice (Figure 5I). As the BBB of the brain and spinal cord are presumed to be identical, the two-photon microscopic data obtained here provide compelling evidence that PBB3 rapidly transits the BBB and neuronal plasma membranes, where it binds to intraneuronal tau inclusions. Accumulation of injected PBB3 in AT8-positive, NFT-like lesions of Tg mice was postmortemly confirmed by ex vivo microscopy (Figures 5J and 5K).

Autoradiographic and PET Imaging of Tau Lesions in PS19 Mice by Radiolabeled PBBs

We investigated the kinetic properties of PBBs by high-performance liquid chromatography (HPLC) analyses of plasma and brain samples collected from non-Tg WT mice treated with these ligands. Following intravenous administration, PBB5 was rapidly converted into a major metabolite, which at 5 min was found at high levels in both plasma and brain extracts. Subsequent liquid

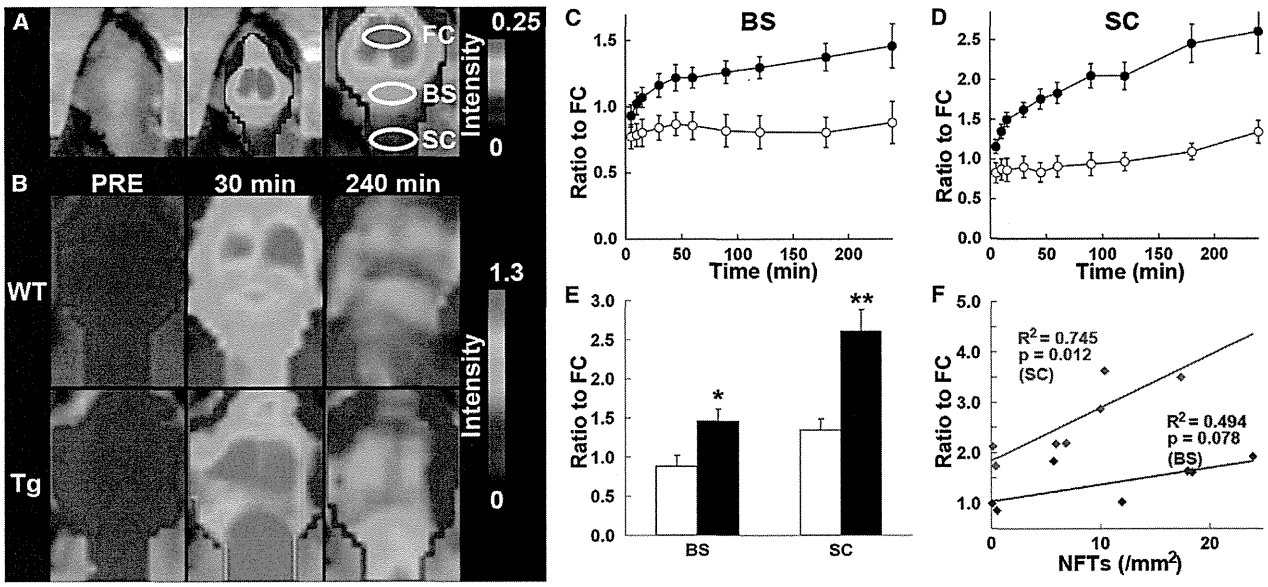

Figure 4. Noninvasive Near-Infrared Imaging of Tau Pathology in Living Tau Tg Mice Using Pulsed Laser Optics and PBB5

(A) Baseline autofluorescence signals (middle) are overlaid on the visible background image of a shaven non-Tg WT mouse head (left). Ellipsoidal ROIs are defined above the frontal cortex (FC), brain stem (BS), and cervical spinal cord (SC) guided by a relatively intense emission from the FC region (right).

(B) Fluorescence intensity maps in 12-month-old WT (top) and PS19 (Tg; bottom) mice before and at 30 and 240 min after the intravenous administration of PBB5 (0.1 mg/kg). The intensity maps (A and B) are normalized by the FC ROI value at 30 min after tracer injection. Long-lasting retention of the tracer was noted in the BS and SC ROIs of the Tg mouse.

(C and D) Target-to-FC ratios of fluorescence intensity in the BS (C) and SC (D) ROIs over the image acquisition time in the WT (open circles; n = 7) and PS19 (closed circles; n = 7) mice. There were significant main effects of time, region, and genotype in two-way, repeated-measures ANOVA (time, $F_{(11, 132)} = 17.6$, $p < 0.001$; region, $F_{(1, 12)} = 29.9$, $p < 0.001$; genotype, $F_{(1, 12)} = 23.6$, $p < 0.001$).

(E) Target-to-FC ratios in the BS and SC ROIs of the WT (open columns) and tau Tg (closed columns) mice at 240 min after tracer injection. *$p < 0.05$; **$p < 0.01$; two-way repeated-measures ANOVA with Bonferroni's post hoc analysis.

(F) Scatterplots of target-to-FC ratios at 240 min versus the number of FSB-positive NFTs per unit area of postmortem 20 μm tissue slices in BS (blue symbols) and SC (red symbols) ROIs of tau Tg mice. Solid lines represent regressions; p values were determined by t test. Vertical bars in the graphs represent SEs.

See also Figures S3 and S4.

chromatography-mass spectrometry (LC-MS) assays suggested that the major metabolite was likely a reduced, electrically neutralized derivative of PBB5 (Figures S5A and S5B). Besides transventricular uptake of unmetabolized PBB5 as implied above, this uncharged form incapable of emitting near-infrared light could readily penetrate the BBB, as well as cell membranes, and thereafter could be reoxidized into its original form, thereby enabling it to bind to tau fibrils, particularly at sites exposed to oxidative stress in pathological conditions. In addition, PBB4 was promptly converted to metabolites capable of entering the brain. Finally, studies of PBB2 and PBB3 showed that they exhibited reasonable biostability and sufficient entry into and clearance from the brain. Indeed, HPLC assays demonstrated that fractions of unmetabolized PBB2 and PBB3 in mouse plasma were 23.5% and 16.3%, respectively, at 3 min after intravenous administration and were 4.6% and 2.8%, respectively, at 30 min. There were also no metabolites of PBB2 and PBB3 detectable in the mouse brain at 3 and 30 min.

We then radiolabeled PBB2 and PBB3 with ^{11}C to conduct autoradiographic and PET assays using PS19 mice. In vitro autoradiography using frozen tissue sections showed binding of these radioligands to the brain stem of PS19 mice and neocortex of AD patients (Figure 6A). As expected from their lipophilicities, [^{11}C]PBB3 yielded high-contrast signals with less nonspecific labeling of myelin-rich white matter than did [^{11}C]PBB2, and the accumulation of [^{11}C]PBB3 in pathological regions was nearly completely abolished by the addition of nonradioactive compounds. Similarly, ex vivo autoradiographic studies demonstrated that intravenously administered [^{11}C]PBB3 selectively labeled the brain stem and spinal cord of PS19 mice harboring neuronal tau inclusions, whereas tau-associated [^{11}C]PBB2 radiosignals were less overt because of a considerable level of nonspecific background (Figure 6B; Figures S6C–S6F). Finally, in vivo visualization of tau lesions in PS19 mouse brains was enabled by a microPET system using these two tracers (Figures 6C, S6A, and S6B). Following intravenous injection, [^{11}C]PBB3 rapidly crossed the BBB and unbound and nonspecifically bound tracers were promptly washed out from the brain with a half-life of ~10 min (left panel in Figure 6E). The retention of [^{11}C]PBB3 signals in the brain stem of 12-month-old PS19 mice lasted over the imaging time (90 min), producing a pronounced difference from that in age-matched non-Tg WT mice (left panel in Figure 6E). By selecting the striatum as a reference region lacking tau deposits, the target-to-reference ratio was estimated for the brain stem, with the value in PS19 mice peaking at around 70 min, contrasting with its continuous decrease over

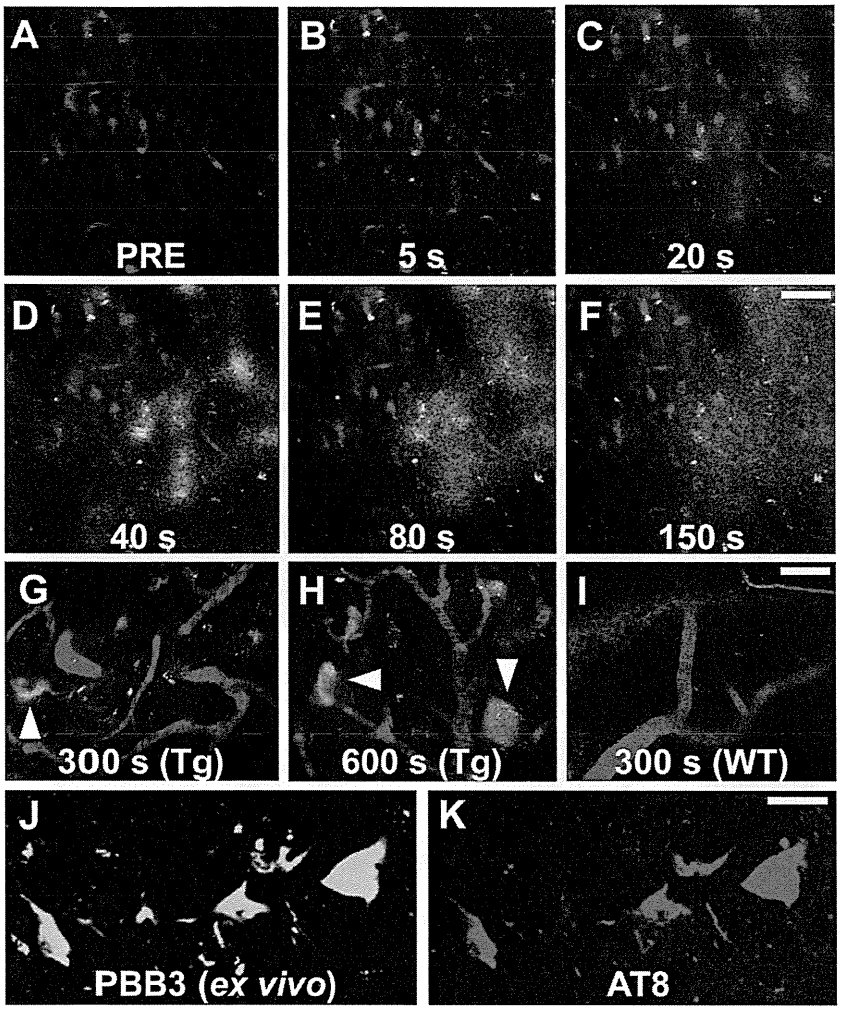

Figure 5. Real-Time Two-Photon Laser Scanning Images of PBB3 Diffusing from Vessels, Binding to Intraneuronal Tau Inclusions, and Clearing from Spinal Cord

(A–H) A maximum projection of fluorescence in a 3D volume of the spinal cord of a living PS19 mouse at 12 months of age before (A) and at various time points after (B–H) intravenous administration of PBB3 (1 mg/kg). Blood vessels were labeled with sulforhodamine 101 (red) intraperitoneally injected at 15 min before PBB3 administration. Green fluorescence indicates a rapid transfer of PBB3 from the plasma to tissue parenchyma (B–E) and subsequent washout from the tissue (F). Background PBB3 signals were further attenuated beyond 300 s, whereas somatodendritic labeling by this compound was observed in a subset of neurons (arrowheads in G and H).

(I) Fluorescence image of WT spinal cord at 300 s after PBB3 injection demonstrates no overt retention of the tracer in the tissue.

(J and K) Ex vivo microscopy for a brain stem section of the same Tg mouse. Tissues were obtained at 60 min after PBB3 injection. Signals of intravenously administered PBB3 (J) overlapped with AT8 immunoreactivity (K).

Scale bars, 50 μm (A–F), 25 μm (G–I), and 25 μm (J and K).

60 min in WT mice (right panel in Figure 6E). The mean ratio at 45–90 min was increased by 40% in 12-month-old PS19 mice as compared with age-matched WT mice ($p < 0.01$ by t test). The agreement between localizations of PET signals and tau inclusions in PS19 mice was proven by postmortem FSB staining of brain sections from scanned mice (Figure 6D). Significantly, the mean target-to-reference ratio in the brain stem quantified by PET correlated closely with the number of FSB-positive inclusions per brain section in the same region of the postmortem sample ($p < 0.001$ by t test; data not shown). [^{11}C]PBB2 exhibited slower clearance from the brain and higher nonspecific retention in myelin-rich regions than [^{11}C]PBB3 (Figure S6G), resulting in insufficient contrast of tau-bound tracers in the brain stem of PS19 mice and a small difference in the target-to-reference ratio of radioactivities between PS19 and WT mice (8% at 45–90 min; $p < 0.05$ by t test; Figure S6H) relative to those achieved with [^{11}C]PBB3.

As radiolabeling at the dimethylamino group in PBB5 with ^{11}C was unsuccessful, ^{11}C-methylation of a hydroxyl derivative of this compound was performed, leading to the production of [^{11}C]methoxy-PBB5 ([^{11}C]mPBB5; Figure S5C). PET images demonstrated complex pharmacokinetics of [^{11}C]mPBB5 (Figures S5D and S5E), and the difference in the specific radioligand binding between Tg and WT mice was small relative to the [^{11}C]PBB3-PET data (Figure S5F). After taking all of these findings into consideration, [^{11}C]PBB3 was selected as the most suitable ligand for in vivo PET imaging of tau pathology in tau Tg mice and human subjects.

Notably, the hippocampus of many PS19 mice was devoid of overt [^{11}C]PBB3 retention (Figure 6C), although a pronounced hippocampal atrophy was noted in these animals. This finding is in agreement with the well-known neuropathological features of PS19 mice in the hippocampus, because the accumulation of AT8-positive phosphorylated tau inclusions results in the degeneration of the affected hippocampal neurons prior to or immediately after NFT formation, followed by the clearance of their preNFTs or NFTs that are externalized into the interstitial CNS compartment (Figure S2). To explore the feasibility of our imaging agents in studies with other tauopathy model mice, we also performed fluorescence labeling with PBBs for brain sections generated from rTg4510 mice (Santacruz et al., 2005; the Supplemental Experimental Procedures). As reported elsewhere (Santacruz et al., 2005), these mice developed numerous thioflavin-S-positive neuronal tau inclusions in the neocortex and hippocampus, and reactivity of these lesions with PBBs was demonstrated by in vitro and ex vivo fluorescence imaging (Figure S7).

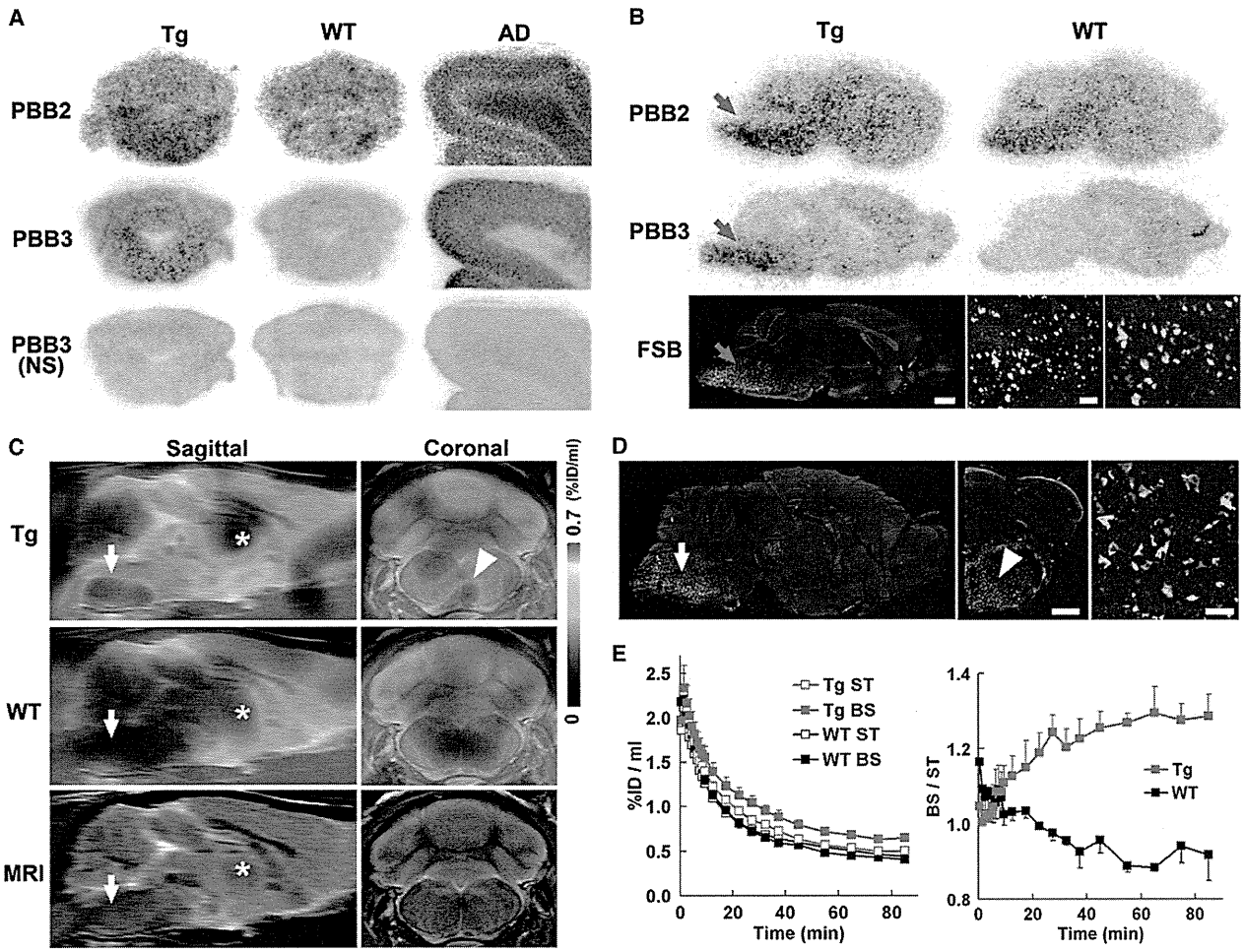

Figure 6. PET and Autoradiographic Detection of Tau Pathologies in PS19 Mice Using [^{11}C]PBB2 and [^{11}C]PBB3

(A) In vitro autoradiograms of PS19 and non-Tg WT hindbrains (coronal sections) and AD frontal cortex. Fibrillar aggregates in the mouse brain stem and AD gray matter produced intense radiolabeling with both tracers, but nonspecific background signals were also observed at a considerably high level with the use of [^{11}C]PBB2. Binding of [^{11}C]PBB3 was profoundly abolished by the addition of nonradioactive PBB3 (10 μM).

(B) Autoradiographic labeling with intravenously injected [^{11}C]PBB2 and [^{11}C]PBB3 in PS19 (Tg) and WT mice. The brains were removed at 45 min after injection and were cut into sagittal slices. The autoradiographic section of PS19 brain was also stained with FSB. Arrows indicate the brain stem containing numerous tau inclusions displayed at intermediate and high magnifications.

(C) Sagittal and coronal PET images generated by averaging dynamic scan data at 60–90 min after intravenous administration of [^{11}C]PBB3. The images are overlaid on the MRI template (images of the template alone are presented at the bottom). Arrows and asterisks indicate the brain stem and striatum, respectively, and arrowhead denotes intense radiolabeling in the medial brain stem of the PS19 mouse.

(D) FSB staining of PS19 mouse brain shown in (C). Sagittal (left) and coronal (middle) images and a high-power view of fibrillar inclusions (right) are displayed. Corresponding to high-level retention of [^{11}C]PBB3 in PET scans, abundant FSB-positive lesions were found in the medial brain stem (arrow and arrowhead).

(E) Time-radioactivity curves (left) in the striatum (ST) and brain stem (BS) and BS-to-ST ratio of radioactivity (right) over the imaging time in PS19 (Tg; red symbols) and WT (black symbols) mice (n = 5 each). Vertical bars in the graphs denote SEs.

Scale bars, 1 cm (A and B, top, middle, and bottom left panels); 1 cm (C and D, left and middle panels); 100 μm (B, bottom middle panel); and 100 μm (B, bottom right panel and D, right panel). See also Figures S5, S6, and S7.

Detection of Tau Pathologies in Living Brains of AD Patients by Comparative PET Imaging with [^{11}C]PBB3 and [^{11}C]PIB

In order to compare the bindings of [^{11}C]PBB3 and [^{11}C]PIB to tau-rich regions in the human brain, in vitro autoradiography was carried out with sections of AD and control hippocampus. A notable difference in labeling between these two radioligands was observed in the CA1 sector and subiculum of the AD hippocampus, where fibrillar tau aggregates predominantly localized to NFTs and neuropil threads (Figure 7A).

We subsequently conducted an exploratory clinical PET study for patients with probable AD (n = 3) and age-matched cognitively normal control (NC) subjects (n = 3). All AD patients exhibited a marked increase in the retention of [^{11}C]PIB in

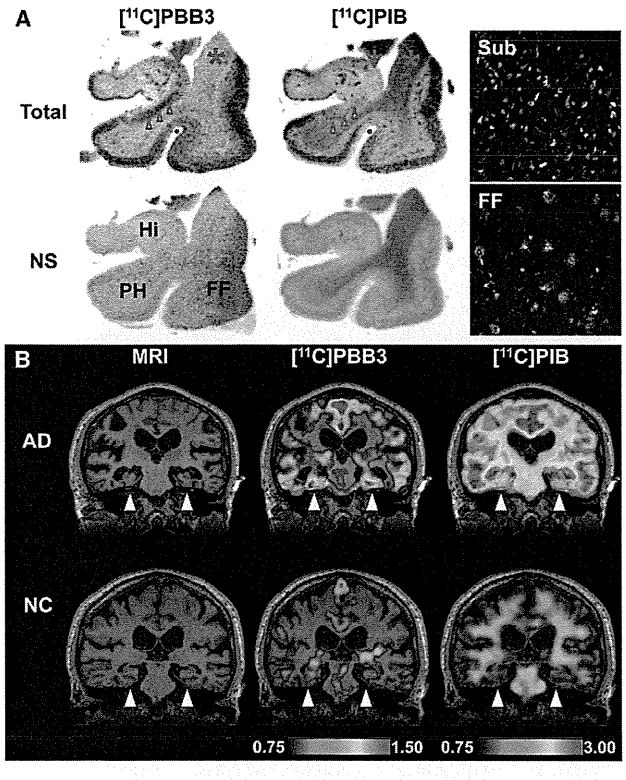

Figure 7. Accumulation of [^{11}C]PBB3 in the Hippocampal Formation of AD Patients Revealed by In Vitro Autoradiography and In Vivo PET

(A) Autoradiographic labeling of adjacent brain sections from an AD patient with 10 nM of [^{11}C]PBB3 (left) and [^{11}C]PIB (middle). The slices contain the hippocampus (Hi), parahippocampal gyrus (PH), fusiform gyrus (FF), and white matter (asterisks). Total binding (top) of [^{11}C]PBB3 and [^{11}C]PIB was markedly abolished (bottom) by addition of nonradioactive PBB5 (100 μM) and thioflavin-S (10 μM), respectively, except for the nonspecific (NS) labeling of white matter with [^{11}C]PIB. The hippocampal CA1 sector and subiculum displayed intense [^{11}C]PBB3 signals without noticeable binding of [^{11}C]PIB, and binding of [^{11}C]PBB3 in cortical areas flanking the collateral sulcus (identified by a red dot) and hippocampal CA2 sector (arrows) was also abundant relative to that of [^{11}C]PIB. FSB staining of amyloid fibrils in the sections used for autoradiography indicated the predominance of NFTs and diffuse plaques in the hippocampal subiculum (Sub) and fusiform gyrus (FF), respectively (right panels), supporting the strong reactivity of [^{11}C]PBB3 with AD NFTs.

(B) MRI (left) and PET imaging with [^{11}C]PBB3 (middle) and [^{11}C]PIB (right) performed in the same AD (top) and normal control (NC; bottom) subjects. Coronal images containing the hippocampal formation (arrowheads) are displayed. [^{11}C]PBB3- and [^{11}C]PIB-PET images were generated by estimating SUVRs at 30–70 min and 50–70 min after radiotracer injection, respectively, and were superimposed on individual MRI data. In the hippocampal formation, prominently increased retention of [^{11}C]PBB3 in the AD patient was in sharp contrast to the modest or negligible changes in [^{11}C]PIB binding as compared with NC. Scale ranges for SUVRs were 0.75–1.50 ([^{11}C]PBB3) and 0.75–3.00 ([^{11}C]PIB).

See also Figure S9.

plaque-rich areas, and all NC were negative for this PET assay. These subjects then received a [^{11}C]PBB3-PET scan, and the [^{11}C]PIB and [^{11}C]PBB3 images were compared in the same individuals. Intravenously injected [^{11}C]PBB3 was delivered to the brain tissue despite its relatively rapid metabolism in humans (Figures 9A and 9B). Unlike [^{11}C]PIB, [^{11}C]PBB3 showed minimal nonspecific binding to white matter and other anatomical structures with high myelin content, although it accumulated in dural venous sinuses in control and AD brains (Figures 7B, 8, and 9B). Time courses of regional radioactivity (Figures 9C and 9D; Figures S8A and S8B) and the standardized uptake value ratio (SUVR) to the cerebellum (Figures S8C and S8D) demonstrated accumulation of [^{11}C]PBB3 in several brain regions of AD patients as compared to controls (definition of these VOIs is indicated in Figure S8E). In agreement with autoradiographic findings, binding of [^{11}C]PBB3 to the medial temporal region, including the hippocampus, contrasted strikingly with the low-level retention of [^{11}C]PIB in this area (Figure 7B). There was a slight increase in the retention of [^{11}C]PBB3 primarily in the medial temporal region of a control subject with a loss of several points in Mini-Mental State Examination (MMSE) (subject 3 in Figure 8), appearing similar to the tau pathology at Braak stage III/IV or earlier (Braak and Braak, 1991), distinct from the lack of enhanced [^{11}C]PIB signals. Indeed, mild increase of medial temporal SUVR (Figure 9E) contrasted with unremarkable change in lateral temporal and frontal SUVRs in this subject (Figures 9G and 9H). Signals of [^{11}C]PBB3 were also intense mainly in the limbic region of a subject with early AD (subject 4 in Figure 8), but profound and moderate increases of SUVRs were also observed in the lateral temporal and frontal cortices, respectively, of this case (Figures 9G and 9H), resembling the localization of tau deposits at Braak stage V/VI (Braak and Braak, 1991). With the further cognitive decline as scored by MMSE (subjects 5 and 6 in Figure 8), additional increase in the retention of [^{11}C]PBB3 was found in the medial temporal region, precuneus, and frontal cortex (Figures 9E, 9F, and 9H). Meanwhile, a substantial decline of [^{11}C]PBB3 binding was noted in the lateral temporal cortex of subject 6 (Figures 8 and 9G). The SUVRs in the medial temporal region, precuneus, and frontal cortex were consequently well correlated with the decline of MMSE scores (Figures 9E, 9F, and 9H). In distinction with [^{11}C]PBB3-PET data, there was no overt association between the binding of [^{11}C]PIB and disease severity in AD patients (Figure 8), consistent with previous observations. These data support the potential utility of [^{11}C]PBB3 for clarifying correlations between the distribution of tau deposition and the symptomatic progression of AD.

As in vitro fluorescence staining indicated that PBB3 was reactive with not only tau lesions but also several types of senile plaques, particularly dense core plaques, density of binding sites, and affinity of [^{11}C]PBB3 for these sites were quantified by autoradiographic binding assays with hippocampal and neocortical sections of AD brains enriched with NFTs and senile plaques, respectively. These analyses demonstrated that specific radioligand binding sites were primarily constituted by high-affinity, low-capacity binding components in NFT-rich regions and low-affinity, high-capacity binding components in plaque-rich regions (Figures S9A and S9B). A subsequent simulation for radioligand binding in an area containing these two types of binding sites at a ratio of 1:1 indicated that the selectivity of [^{11}C]PBB3 for NFTs versus plaques may be inversely associated with concentration of free radioligands (Figure S9C). In a range of free concentration in the brain achievable

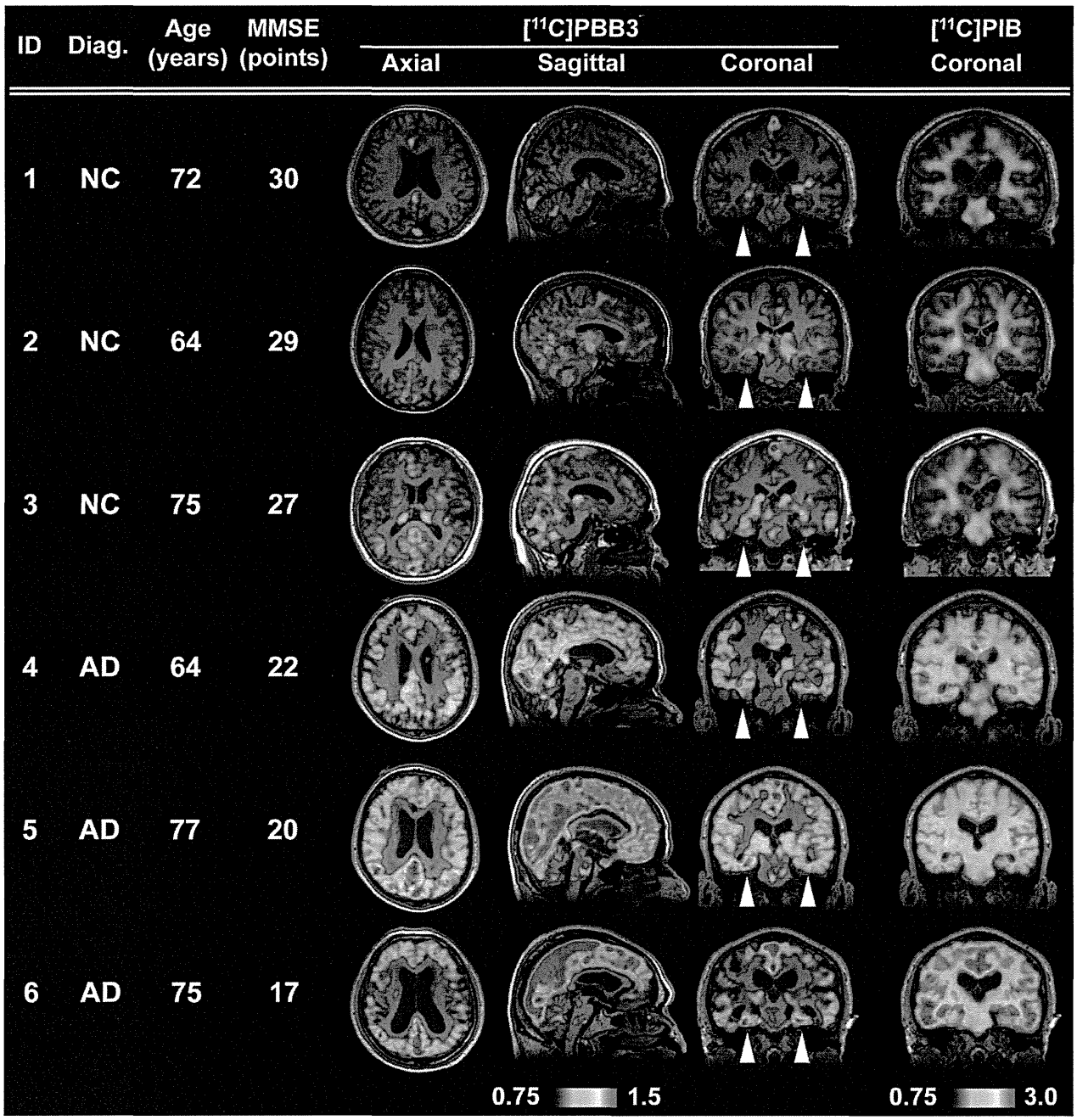

Figure 8. Orthogonal [^{11}C]PBB3-PET Images in All Human Subjects Examined in the Present Exploratory Clinical Study

Data are displayed as parametric maps for SUVR. The [^{11}C]PBB3 binding to the hippocampal formation (arrowheads) was increased consistently in AD patients in contrast to minimum radiotracer retention in normal control (NC) subjects with MMSE scores of 29–30 points (subjects 1 and 2). Another NC subject with an MMSE score of 27 points (subject 3) was negative for [^{11}C]PIB-PET but exhibited slight accumulation of radiotracer signals primarily around the hippocampus, resembling fibrillar tau deposition at Braak stage III/IV or earlier. Sagittal slices around the midline illustrate that radioligand signals were the most intense in the limbic system but began to expand to the neocortex in a patient with the mildest AD (subject 4), in agreement with the tau pathology at Braak stage V/VI, and was further intensified in most neocortical areas, corresponding to Braak stage VI, apparently as a function of the disease severity assessed by MMSE (subjects 5 and 6). The AD patient with the lowest MMSE score (subject 6) displayed a less profound increase of [^{11}C]PBB3 retention in the lateral temporal and parietal cortices than did the other two AD cases, and this is attributable to marked cortical atrophy in this individual and/or toxic loss of tau-bearing neurons in these brain areas at an advanced pathological stage. In contrast to the spatial profiles of [^{11}C]PBB3 binding, the distribution of [^{11}C]PIB signals appeared unchanged among AD subjects. See also Figure S9.